Ice and gas in protostellar clouds and planet-forming disks: a combined laboratory and observational study

Terwisscha van Scheltinga, J.

Citation

Terwisscha van Scheltinga, J. (2021, November 30). *Ice and gas in protostellar clouds and planet-forming disks: a combined laboratory and observational study.* Retrieved from https://hdl.handle.net/1887/3245869

6 | FORMATION OF CO_2 THROUGH CONSUMPTION OF GAS-PHASE CO ON VACUUM-UV IRRADIATED WATER ICE

Jeroen Terwisscha van Scheltinga, N.F.W. Ligterink, A.D. Bosman, Michiel R. Hogerheijde, Harold Linnartz, Submitted to Astronomy & Astrophysics

Abstract

Recent observations of protoplanetary disks suggest that they are depleted in gas-phase CO up to a factor of 100 with respect to predictions from physical-chemical (or thermo-chemical) models. It has been posed that gas-phase CO is chemically consumed and converted into less volatile species through gas-grain processes. Observations of interstellar ices reveal a CO_2 component in a polar (H_2O) ice matrix, suggesting potential co-formation or co-evolution.

The aim of the work in this chapter is to experimentally verify the interaction of gas-phase CO with solid-state OH radicals on the surface of water ice above the sublimation temperature of CO.

For this amorphous solid water (ASW) is deposited in an UHV setup and irradiated with vacuum-UV (VUV) photons (140–170 nm, produced with a microwave discharge hydrogen lamp) to dissociate H_2O and create OH radicals. Gas-phase CO is simultaneously admitted and only adsorbs with a short residence time on the ASW. Formed products are studied both in the infrared through Fourier transform infrared spectroscopy and quadrupole mass spectrometry.

The experiments presented in this chapter show that gas-phase CO is converted into CO_2 when interacting with ASW that is VUV irradiated in the temperature range of 40–120 K. Between 40 and 90 K, CO_2 production is constant, above 90 K, CO_2 production is reduced in favor of O_2 production. In the temperature range of 40–60 K, the CO_2 remains in the solid state, while at temperatures ≥ 70 K the majority of the formed CO_2 is released into the gas phase.

At the end of this chapter we conclude that gas-phase CO reacts with OH radicals, created on the surface of ASW with VUV irradiation, above its canonical sublimation temperature. The diffusion during the short, but nonzero, residence times of CO on the surface of ASW suggests that a Langmuir-Hinshelwood type reaction is involved. Formation of CO_2 is seen up to 120 K, with a constant production at 40–90 K, gradually yielding to O_2 production at higher temperatures. This mechanism could explain (part of) the observed presence of CO_2 embedded in water-rich ices when it occurs during the build up of the H_2O ice mantle. It may also contribute to the observed lack of gas-phase CO in planet-forming disks, as previously suggested. It should be noted though that our experiments indicate a lower efficiency than originally adopted in model descriptions of planet-forming disks.

6.1   Introduction

In typical laboratory astrochemistry experiments the processes that occur in the solid state and gas phase are investigated independently. However, there are conditions in the interstellar medium where these are intimately intertwined and could potentially affect each other. In this work, we explore experimentally the interaction between gas-phase carbon monoxide (CO) and UV irradiated water ice (H_2O) and place the results in astrophysical context.

In the study of planet forming disks, CO and its isotopes are common tracers of the total gas mass, but are often found to be depleted by factors up to 10–100, even after taking into account freeze-out of CO in the coldest disk regions (Ansdell et al. 2016; Miotello et al. 2017; Trapman et al. 2021). Recent chemical models by Bosman et al. (2018) suggest that gas-phase CO could be converted into CO_2 after interaction with a UV-irradiated H_2O ice surface, at temperatures just above the CO sublimation temperature. Under realistic disk conditions, this pathway was found by Bosman et al. (2018) to convert significant amounts of CO into CO_2. However, little experimental work exists to confirm this mechanism. If efficient, the UV-irradiated edges of molecular clouds could be another environment where this gas-grain reaction can occur. This could possibly explain (part of) the observed presence of CO_2 in polar ices (Pontoppidan et al. 2008), if gas-phase CO conversion happens on the surface during the build up of the H_2O ice mantle and adding to contributions from other pathways already studied.

The solid-state formation of CO_2 has been investigated both theoretically (see e.g., Goumans et al. 2008; Goumans & Andersson 2010; Arasa et al. 2013) and experimentally resulting in several energetic and non-energetic pathways:

1. Ground-state CO reacts with an electronically excited CO* to form CO_2 and atomic carbon (Gerakines et al. 1996; Palumbo et al. 1998; Loeffler et al. 2005; Jamieson et al. 2006; Bennett et al. 2009; Ioppolo et al. 2009),

2. CO reacts with atomic oxygen to form CO_2 (Roser et al. 2001; Madzunkov et al. 2006; Raut & Baragiola 2011; Ioppolo et al. 2013; Minissale et al. 2013),

3. CO reacts with a hydroxyl (OH) radical to form CO_2 and atomic hydrogen (Watanabe & Kouchi 2002b; Watanabe et al. 2007; Ioppolo et al. 2009; Oba et al. 2010, 2011; Ioppolo et al. 2011; Noble et al. 2011; Zins et al. 2011; Yuan et al. 2014),

4. Formaldehyde (H_2CO) reacts with atomic oxygen and forms CO_2 and molecular hydrogen (Minissale et al. 2015).

All of the above pathways efficiently produce CO_2 in the solid state and only the last pathway does not include CO. The majority of these solid-state experiments are performed at temperatures below 20 K, representative of dark cloud or disk midplane (> 20 AU) conditions. This is well below the CO sublimation temperature, which is approximately 20 and 30 K for interstellar and laboratory timescales, respectively. The low temperatures in these experiments ensure that CO stays adsorbed on the surface and is able to react with the other ice constituents. The experimental studies by Oba et al. (2011) and Yuan et al. (2014) have investigated the formation of CO_2 from CO at substrate temperatures above the sublimation temperature of CO. In the

former, CO_2 was formed when CO and OH radicals were co-deposited on a substrate in the temperature range from 40 to 60 K. The latter observed formation of CO_2 when gas-phase CO interacted with OH radicals produced by UV photons on the surface of water ice at 76 K. Both works show that CO can interact with OH radicals in the solid state above its canonical desorption temperature.

In this work, we set out to experimentally investigate the conversion of gas-phase CO into CO_2 on the surface of vacuum-UV (VUV) irradiated water ice (40–120 K), and asses the efficiency in astrophysical settings. Specifically, amorphous solid water (ASW) is irradiated at a temperature of the ASW, ≥ 40 K, which ensures that the majority of the gas-phase CO in our experimental chamber does not freeze-out onto our ASW sample. Section 6.2 describes the methods used to investigate this process, and analyze the data. Results are written down in Section 6.3 and are discussed in Section 6.4. The astrophysical implications are given in Section 6.5, and concluding remarks are written down in Section 6.6.

6.2 Methods

6.2.1 CryoPAD2

All reported laboratory measurements are performed in the Leiden Laboratory for Astrophysics using CryoPAD2 (Chapter 2, Ligterink et al. 2017, 2018b). This setup operates under ultra-high vacuum conditions ($P_{mc} \sim 5 \times 10^{-11}$ mbar at 15 K). It accommodates a gold-coated substrate which is positioned in the center of a stainless steel chamber and acts as an analogue for an interstellar dust grain surface. On top of the chamber a closed-cycle helium cryostat is positioned which cools the gold-coated surface down to temperatures of 15 K. A Lakeshore 350 temperature controller sets the temperature of the surface through PID-controlled Joule heating in the range of 15 to 300 K with an absolute and relative accuracy of 2 and 1 K, respectively. In order to further simulate the interstellar environments in which these dust grains reside, a microwave-discharge hydrogen-flow lamp (MDHL) is connected to the chamber. These type of sources generally produce VUV photons at 121.6 nm, Lyman-α, and between 140 to 170 nm, which corresponds to photon energies of 7.5 to 10.2 eV. However, in the present experiments a MgF_2 window is used which absorbs Lyman-α photons, see Appendix 6.A for the UV spectrum. The flux of the MDHL at the location of the substrate is determined with a NIST-calibrated photodiode (SXUV-100) as $(2.5 \pm 0.3) \times 10^{14}$ photons s^{-1} cm^{-2}.

The reactions induced by VUV irradiation under these conditions are diagnosed using InfraRed (IR) spectroscopy and mass spectrometry. The collimated beam of a Fourier-Transform InfraRed Spectrometer (Agilent 660 FTIRS), is used for Reflection Absorption InfraRed Spectroscopy (RAIRS). In this method the incoming FTIR beam is reflected from the substrate under a grazing incidence angle, improving the sensitivity. This *in situ* diagnostic allows us to probe, qualitatively and quantitatively, the molecular content in the ice adsorbed on the substrate. The infrared spectra are acquired continuously during the experiments to investigate and track the chemical evolution in the solid state under the influence of VUV irradiation.

The second diagnostic tool is a Hiden HAL/3F PIC 1000 series quadrupole mass spectrometer (QMS). During VUV irradiation some molecular species desorb from the substrate into the gas phase. The QMS probes the molecular content of the

Table 6.1: Overview of the performed experiments.

Series	Molecules	Temp[a] (K)	H_2O col. den.[b] (monolayers)	Notes
Main experiments	$H_2{}^{18}O$ (s) + $^{13}C^{18}O$ (g)	40 (15)	57.8	–
	$H_2{}^{18}O$ (s) + $^{13}C^{18}O$ (g)	50 (15)	56.7	–
	$H_2{}^{18}O$ (s) + $^{13}C^{18}O$ (g)	60 (15)	57.6	–
	$H_2{}^{18}O$ (s) + $^{13}C^{18}O$ (g)	70 (15)	61.8	–
	$H_2{}^{18}O$ (s) + $^{13}C^{18}O$ (g)	80 (15)	62.9	–
	$H_2{}^{18}O$ (s) + $^{13}C^{18}O$ (g)	90 (15)	57.8	–
	$H_2{}^{18}O$ (s) + $^{13}C^{18}O$ (g)	100 (15)	56.8	–
	$H_2{}^{18}O$ (s) + $^{13}C^{18}O$ (g)	120 (15)	58.3	–
Control experiments	$H_2{}^{18}O$ (s)	40 (15)	70.2	Water only.
	$H_2{}^{18}O$ (s) + ^{13}CO (g)	60 (15)	63.2	$^{13}C^{16}O$.
	$H_2{}^{18}O$ (s) + $^{13}C^{18}O$ (g)	40 (15)	66.4	No VUV.

Notes. [a] The first temperature is the temperature at which the ASW is VUV irradiated and the second temperature in parenthesis is the deposition temperature. [b] The H_2O column density is derived through the integrated area of the OH-stretching mode (boundaries, 3800–2950 cm^{-1}) through Eq. 6.1, where A' is taken to be 1.5×10^{-16} cm molec^{-1} ($H_2{}^{16}O$, Bouilloud et al. 2015).

atmosphere in the chamber. This allows for qualitative assignment of species released and/or produced during the experiments through their characteristic mass fragmentation patterns. Furthermore, after calibration of the QMS through the procedure described in Section 6.2.3.2, it is possible to derive the quantitative amount of a species released into the gas phase. After VUV irradiation, the substrate temperature is linearly increased with time in a temperature programmed desorption (TPD) experiment until all adsorbed species have thermally desorbed. During TPD, species are released into the gas phase at their canonical desorption temperature, and are subsequently measured by the QMS. Upon ionization, in our case with 70 eV electrons, molecules fragment into a characteristic fragmentation pattern, which allows for assignment of newly formed species, complementary to the IR. Isotopically enriched precursors are used to discriminate from background gas contributions and to add additional diagnostic information to the RAIRS and TPD experiments.

6.2.2   Experimental protocol

The following molecules are used in the experiments: Milli-Q H_2O (Type I), $H_2{}^{18}O$ (Sigma-Aldrich, 97%), regular CO (Linde gas, 99.997%), and $^{13}C^{18}O$ (Sigma-Aldrich, 99% ^{13}C and 95% ^{18}O). The experiment is started by depositing a layer of ASW onto the substrate. The gas-phase H_2O enters the chamber roughly 1 cm away from the substrate, and is deposited under normal incidence to the substrate. The temperature of the substrate during H_2O deposition is set at 15 K. This ensures that the deposited H_2O is porous-ASW. A precision leak valve is used to guarantee consistent column densities of H_2O throughout the measurements. Before the experiments continue, the chamber is left to settle for at least 30 minutes. This ensures that the pressure in the

main chamber (P_{mc}) is below 2.0×10^{-10} mbar and that the amount of residual gas-phase H_2O can be neglected. After this, the substrate temperature is slowly increased to a specific temperature at which the experiments are performed, typically with a rate of 2 K min^{-1}. Once the desired sample temperature is reached, the MDHL is started and gas-phase CO is released into the chamber. The gas-phase CO enters the chamber at roughly 5 cm distance from the substrate, and under 45 degrees with respect to the substrate normal. The precision leak valve is set to have a constant P_{mc} of 5.0×10^{-8} mbar. This translates into the ASW surface being exposed to approximately 5×10^{13} CO molecules cm^{-2} s^{-1}. The ASW is exposed in total 300 minutes to VUV irradiation (with a total incident fluence of 4.5×10^{18} photons) and CO molecules, after which TPD is performed to sublimate parent and newly-formed species. During VUV irradiation the shutter between the MDHL and vacuum chamber is closed to measure the baseline signals of the chamber without VUV irradiation. A list of experiments performed in this study is given in Table 6.1, which also provides information on the variable experimental parameters.

6.2.3   Data analysis

6.2.3.1   RAIRS vibrational spectroscopy

The infrared spectra are acquired in RAIRS mode with the FTIR and are subsequently analysed. The column density, $N_{species}$, of the probed molecules on the substrate is derived through the following relationship with the measured absorbance

$$N_{species} = \ln(10) \cdot \frac{\int_{band} \log_{10} \left(\frac{I_0(\tilde{\nu})}{I(\tilde{\nu})} \right) d\tilde{\nu}}{R \cdot A'}, \tag{6.1}$$

where the absorbance, the ratio of the incoming flux, $I_0(\tilde{\nu})$, and reflected flux, $I(\tilde{\nu})$, is integrated over a range that encompasses the full absorption feature, and A' is the apparent band strength. The apparent band strengths are taken from literature from transmission experiments; for RAIRS these values need to be corrected with a value R in order to retrieve accurate column densities. The RAIRS correction factor is determined through isothermal desorption of CO and results in a setup-specific value (see e.g., Öberg et al. 2009c). We assume that the area probed by the infrared beam on our substrate amounts to 1.0 cm^2 and thus the amount of molecules, $N_{species}$, is also the column density, given in molecules cm^{-2}. As stated before and shown in Table 6.1, all main experiments are performed with $^{13}C^{18}O$ and $H_2^{18}O$ resulting in the formation of $^{13}C^{18}O_2$. To our knowledge the apparent band strength of this specific isotope of CO_2 is unknown and thus the apparent band strength of $^{13}CO_2$, 6.8×10^{-17} cm molecule^{-1} (Bouilloud et al. 2015), is used to approximate the column density of $^{13}C^{18}O_2$.

As will be shown in Section 6.3, multiple CO_2 features are observed in the IR. In order to follow the growth of these different CO_2 features, the three prominent ones are approximated by fitting a Gaussian profile to each of them in order to deconvolve the spectra. The CURVE_FIT function from SCIPY is used to fit a Gaussian profile to each absorption component through least squares regression (Virtanen et al. 2020). A 3-Gaussian fit reproduces the integrated absorbance to $\leq 10\%$, and suffices as a fit, given the variation in observed profile shapes due to (small) changes in physical/chemical environment and spectroscopic artifacts in the spectra.

6.2.3.2   QMS calibration

RAIRS allows determination of the column density in the solid state, while the QMS allows tracing of molecules released from the solid state into the gas phase. In order to use the QMS for quantitative purposes mass signals need to be calibrated and this is realized, through the photodesorption of CO (see e.g., Fayolle et al. 2013; Martín-Doménech et al. 2015). The loss of CO in the solid state, which is traced with RAIRS, is correlated to the CO signal measured by the QMS. This calibration allows for the conversion of any CO QMS signal, released under VUV irradiation, to a CO column density released from the solid state. For other molecules, one needs to take into account the partial electron-impact ionization cross section, and the mass sensitivity of the molecule in question with respect to CO. The following relation is used to quantify the amount of CO_2 formed and released into the gas phase

$$N_{CO_2} = S_{CO_2} \cdot \frac{\sigma_{CO}}{\sigma_{CO_2}} \cdot \frac{F(CO^+/CO)}{F(CO_2^+/CO_2)} \cdot \frac{M(CO)}{M(CO_2)} \cdot \frac{N_{CO(ice)}}{S_{CO(gas)} \, t}, \qquad (6.2)$$

where N_{CO_2} is the column density of CO_2 released from the solid state, σ the total electron-impact ionization cross-section, F the fragmentation fraction of the ionized species, and M the mass sensitivity function of the QMS. The variables in the last term of Eq. 6.2 are determined in a separate experiment where $N_{CO(ice)}$ is the amount of CO that desorbs from the solid state due to photodesorption measured by the FTIRS, S_{CO} the measured CO signal by the QMS, and t the time over which the $N_{CO(ice)}$ photodesorbed.

6.3   Results

In this section we present the results of the experiments mentioned in Table 6.1. In general, irradiation of ASW with VUV photons in the presence of gas-phase CO produces CO_2. Additionally, in the experiments at the higher end of the temperature range, (> 90 K), formation of molecular oxygen (O_2) is observed. To understand the processes that occur on and/or in the solid state we consider the infrared and QMS results, and how these change with temperature.

6.3.1   Infrared spectroscopy results

We observe the formation of CO_2 in the solid state through RAIRS. In Figure 6.1 we present five difference RAIRS spectra at experimental temperatures of 40 and 60 K. Such spectra are obtained by subtracting the initial ASW spectrum, before VUV irradiation, from the subsequently acquired spectra during irradiation. The spectra shown here are obtained at five different VUV fluence intervals where ASW was simultaneously exposed to gas-phase CO. It is apparent from these spectra that three distinct absorption features grow with increasing VUV fluence. The three features are positioned at 2279, 2260, and 2243 cm^{-1} and are all attributed to CO_2, namely $^{13}C^{18}O_2$ cluster islands on top of the water ice, $^{13}C^{16}O^{18}O$ bound to water, and $^{13}C^{18}O_2$ bound to water, respectively (Lehmann et al. 1977; He et al. 2017). The ^{16}O in $^{13}C^{16}O^{18}O$ originates from isotope impurities in the $H_2^{18}O$ and $^{13}C^{18}O$ samples.

The lowest ASW temperature at which the experiments are performed is 40 K. This ensures that the majority of the gas-phase CO molecules that enter the vacuum
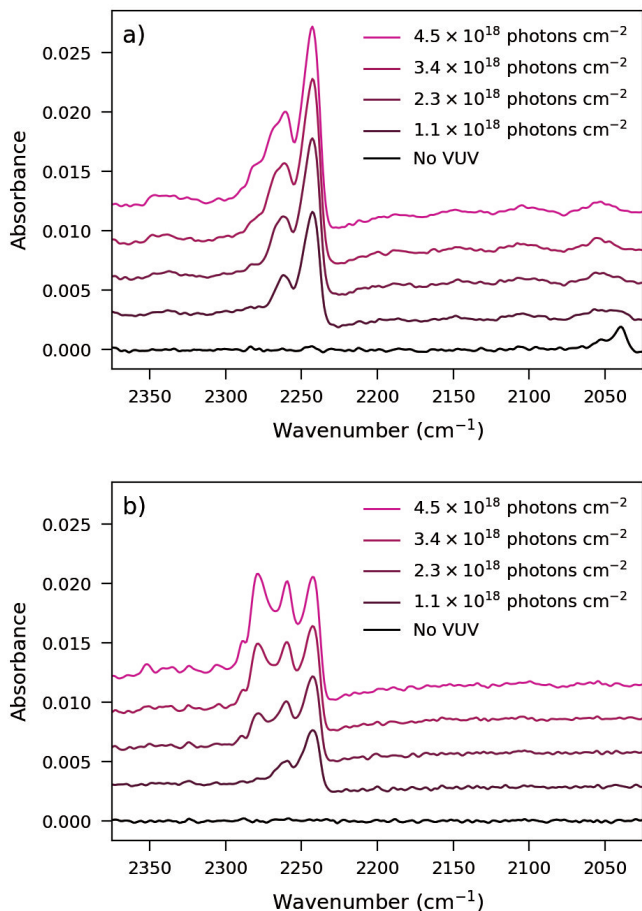
Figure 6.1: Five difference RAIRS spectra following VUV irradiation of ASW ($H_2{}^{18}O$) at 40 K (top) and 60 K (bottom) with gas-phase $^{13}C^{18}O$ at different VUV fluences, increasing from low to high.

chamber cannot adsorb onto our sample, as it is above the canonical desorption temperature of CO. However, as is shown by He et al. (2016b), the sticking coefficient of CO on nonporous-ASW (np-ASW) is close to unity at 40 K. Once the ASW is covered with CO, no additional CO freeze-out occurs. This is seen in the experiment at 40 K through the infrared signal around 2040 cm^{-1} where, preceding VUV-irradiation, the ASW is briefly exposed to gas-phase CO only (Figure 6.1a). In this short 5 minute window, CO adsorbs on top of the ASW with a column density of ~ 1.1 monolayers, where one monolayer equals 10^{15} molecules cm^{-2}. This ice grows within 60 s and does not further increase. As soon as VUV irradiation starts, this solid-state CO on the surface of the ASW is consumed. At ASW temperatures ≥ 50 K no adsorption of CO is seen (Figure 6.1b). This is expected as the sticking coefficient of CO on ASW significantly drops at temperatures ≥ 50 K. An upper limit of ≤ 0.1 monolayers is derived for CO on top of ASW at temperatures ≥ 50 K.

Figure 6.2 shows the combined results of the experiment with ASW at 40 K. The upper and lower panels show results of both the infrared and QMS experiments during VUV irradiation and TPD, respectively. Figure 6.2a shows the growth of the combined and each individual CO_2 component during VUV irradiation (shaded areas), while
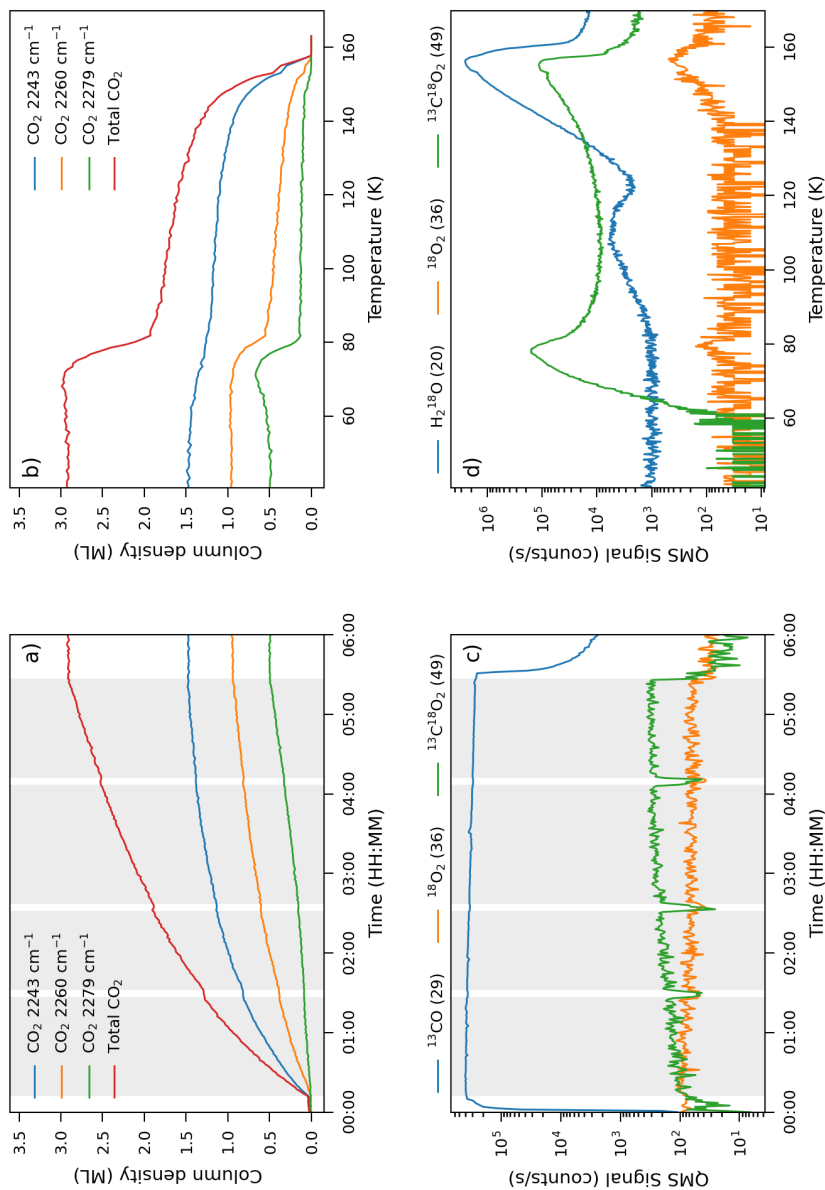
Figure 6.2: Results of the experiment of ASW at a temperature of 40 K. In the top row the deconvolved infrared components are given and in the bottom row the data for the quadrupole mass spectrometer (QMS) is presented. The left column shows data acquired during VUV irradiation (shaded area is with VUV shutter open) and on the right during temperature programmed desorption (TPD). ^{13}CO is shown in panel c), as measuring the main isotope ($^{13}C^{18}O$) would saturate the QMS and the ^{16}O isotope is present in the CO sample at a level of 5‰.

Figure 6.2b shows the decrease, but during TPD. It is evident that the deconvolved components grow at different rates. The CO_2 component at 2243 cm^{-1} is the first to grow and levels off as the VUV fluence increases. This component is attributed to $^{13}C^{18}O_2$ bound to the ASW surface, as this initial CO_2 can only interact with the ASW. The 2279 cm^{-1} component has a delayed start and is attributed to $^{13}C^{18}O_2$ clusters on the surface of ASW (cf. He et al. 2017, who observed the same features, but shifted by ~ 100 cm^{-1} due to the isotope shift.) As the ASW temperature increases, the diffusion of CO_2 also increases. The growth of CO_2 clusters starts earlier and the amount of molecules in clusters is increased with ASW temperature, see Figures 6.2, 6.8 (50 K), and 6.9 (60 K). Additionally, due to the increased temperature of the ASW, less binding sites are occupied by CO_2 due to reduced residence times. This is reflected in less CO_2 molecules bound to the ASW and more CO_2 molecules in clusters with increasing temperature. The component at 2260 cm^{-1} is due to $^{13}C^{16}O^{18}O$, formed from isotope impurities, on the ASW surface. Additionally, in the fitting of these three CO_2 components the 2260 cm^{-1} component comprises contribution from the 2243 and 2279 cm^{-1} features, as a Gaussian profile does not accurately represent these solid-state CO_2 absorption features. This makes an unique assignment for the 2260 cm^{-1} component difficult.

The decrease of the total CO_2 and each of the separate components during TPD is shown in Figure 6.2b. The CO_2 sublimates in two steps, the first desorption event occurs at ~ 80 K and the second at ~ 150 K. The former is in line with the canonical desorption temperature of CO_2, and the latter with the canonical desorption temperature of H_2O. The component at 2279 cm^{-1} drops around ~ 80 K, which is in line with clusters of CO_2. The component at 2243 cm^{-1} gradually drops as the temperature of the ASW increases and disappears with the desorption of H_2O at 156 K, which is in agreement with CO_2 bound to ASW surface.

At ASW temperatures ≥ 70 K, the majority of the formed CO_2 is released back into the gas phase (see e.g., Figure 6.3). At 70 and 80 K, however, some of the initially formed CO_2 remains in the solid state, see Figure 6.3a and Appendix 6.10a, respectively. This CO_2 is formed during the initial moments of VUV irradiation and is bound to the deep binding sites on the ASW surface that are able to "trap" CO_2. The column densities of trapped CO_2 at 70 and 80 K are 0.6 and 0.12 monolayers, respectively. No solid-state CO_2 is detected in the experiments with ASW temperatures ≥ 90 K, and the upper limit of solid-state CO_2 is derived to be ≤ 0.02 monolayers.

6.3.2 QMS results

The QMS allows tracing of gas-phase species in the chamber during VUV irradiation and afterwards during TPD. The signals measured during TPD are only used for identification. In the following two sections we focus first on the QMS analysis of CO_2 that remained in the solid state (40–60 K) and then on CO_2 released into the gas phase (> 60 K) after formation.

6.3.2.1 Solid-state CO_2 (40–60 K)

The majority of the CO_2 formed at ASW temperatures of 40–60 K remains in the solid state, as is found in the infrared experiments. This solid-state CO_2 is released into the gas phase during TPD due to thermal desorption, and subsequently measured with the QMS. However, during VUV irradiation there is some gas-phase CO_2 signal
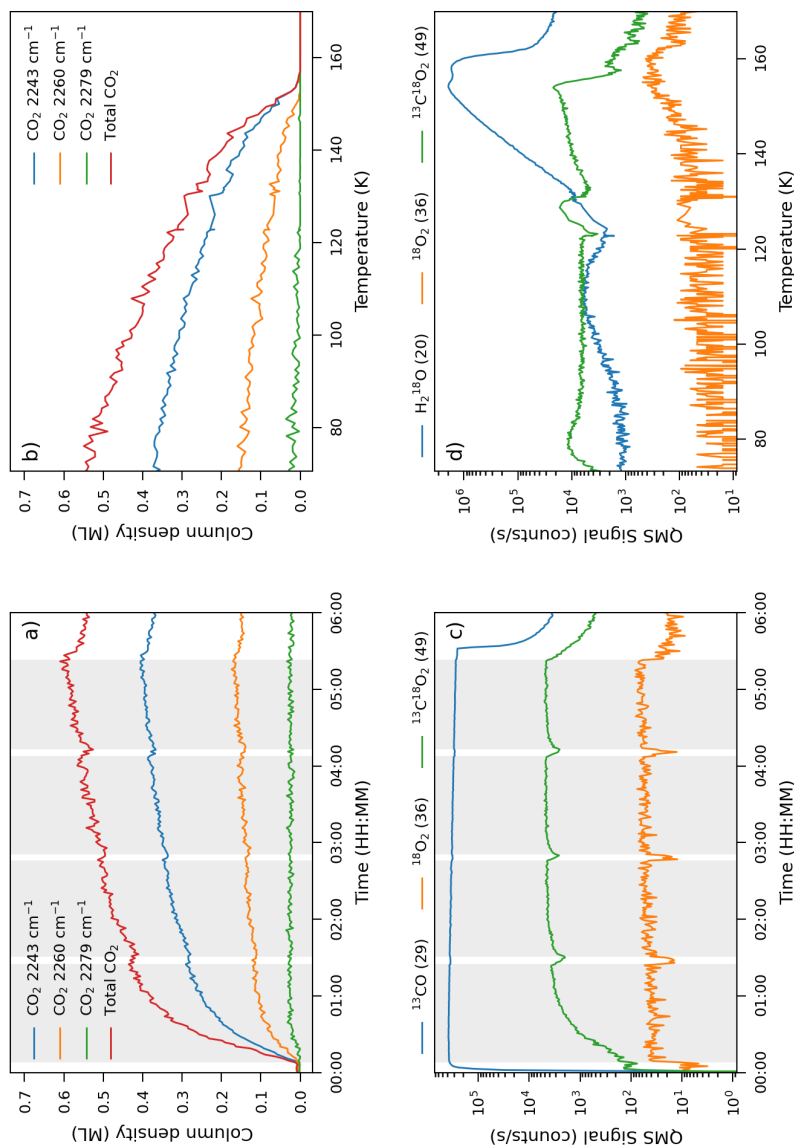
Figure 6.3: Results of the experiment of ASW at a temperature of 70 K. In the top row the deconvolved infrared components are given and in the bottom row the data for the quadrupole mass spectrometer (QMS) is presented. The left column shows data acquired during VUV irradiation (shaded area is with VUV shutter open) and on the right during temperature programmed desorption (TPD). ^{13}CO is shown in panel c). ^{13}CO is present in the CO sample at a level of 5%. The increased measuring the main isotope (^{13}C^{18}O) would saturate the QMS and the ^{16}O isotope is present in the CO sample at a level of 5%. The increased signal in panel d) during the TPD between 120–130 K is due an unfortunate nonlinear temperature artifact.

measured by the QMS. This is illustrated in Figure 6.2c (shaded areas) by the signal at mass-to-charge ratio $(m/z) = 49$, which is associated with the main mass-fragmentation peak of $^{13}C^{18}O_2$. The increase of this CO_2 QMS signal follows approximately the same trend as the growth of the CO_2 column density measured in the infrared (Figure 6.2a). When the VUV shutter is closed, unshaded areas, the signal at $m/z = 49$ drops. We attribute this gas-phase CO_2 QMS signal to photodesorbed CO_2 from the solid state (Fillion et al. 2014).

During TPD, there are two distinct desorption peaks of CO_2 with an elevated plateau between them (see e.g., Figure 6.2d). The first desorption peak occurs at 78 K, the canonical desorption temperature of CO_2. The CO_2 molecules that desorb at this temperature, are those in CO_2 cluster islands. The second desorption peak coincides with the water desorption peak observed at 156 K. Both are in agreement with the deconvolved infrared components at 2279 and 2243 cm^{-1} (see e.g., Figure 6.2b).

6.3.2.2   Gas-phase CO_2 (> 60 K)

In the remainder of the main experiments, Figures 6.3, 6.10–6.13, the temperature of the ASW ranges from 70–120 K. During these experiments equal amounts of CO are converted into CO_2. However, the majority of the formed CO_2 is released into the gas phase after formation. Similar to Figure 6.2, we present the results of ASW at 70 K in Figure 6.3. During this experiment $\sim 20\%$ of the formed CO_2 stays on the surface of ASW, while the remainder is released into the gas phase. The release of CO_2 into the gas phase is slightly below the canonical CO_2 desorption temperature, 78 K. This is no surprise as the binding energy of CO_2 bound to H_2O equals 2250 K, while the binding energy between CO_2 molecules is higher at 2415 K (He et al. 2017). During the first hour of VUV irradiation, the ASW surface "traps" some of the formed CO_2 in its deep binding sites, but once these are occupied, most of the subsequently formed CO_2 is released into the gas phase. This is reflected by the initial rapid build up of CO_2 in the infrared during the first VUV irradiation interval (Figure 6.3a). Additionally, in Figure 6.3c it is shown that the gas-phase CO_2 builds up during the initial VUV interval, where it reaches steady state at the same time when the growth of solid-state CO_2 levels off. Lastly, during TPD the two main desorption features clearly appear, but not as prominent as in the 40–60 K experiments. The majority of the CO_2 is released during TPD in the "plateau" region between 85–145 K, that is, between the canonical desorption of CO_2 cluster islands and H_2O, as is shown in Figure 6.3d.

In the experiments with ASW temperatures between 90 and 120 K (Figures 6.11–6.13), no solid-state CO_2 is observed in the infrared (column density $\leq 2.0 \times 10^{13}$ cm^{-2}). The TPDs in this temperature range, however, do reveal that some CO_2 is still bound to the surface of the ASW. Following the trend as seen in the experiments with ASW at 70 and 80 K, the amount of CO_2 that remains on the ASW surface decreases with increasing temperature, see Figures 6.11–6.13. This is in line with the decrease of absolute signal of the "plateau" during TPD. Interestingly, a significant amount of O_2 formation is observed in this temperature range, as shown by the QMS signal at $m/z = 36$ representing $^{18}O_2$. The formation of O_2 increases with temperature at the cost of CO_2. At 120 K the formation of CO_2 is almost completely quenched and over 90% of the formed products is O_2.

Figure 6.4: Column densities of the formed products when ASW is VUV irradiated and exposed to gas-phase CO as function of temperature. Solid-state column densities are derived through FTIRS and gas-phase column densities through the QMS as described in Section 6.2.3.
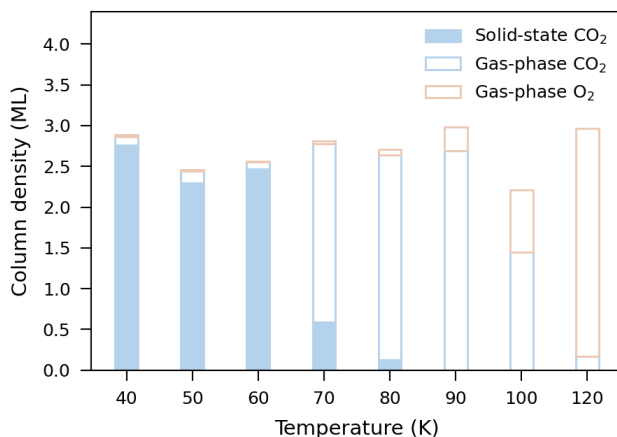
6.3.3 CO_2 and O_2 column densities

For each of the main experiments the column densities of the products are summarized in Figure 6.4. The column density of solid-state CO_2 is derived through the combined integrated absorbance area of the three infrared CO_2 features. The CO_2 and O_2 gas-phase column densities are derived through the calibration of the QMS described in Section 6.2.3.2. In short, in the temperature range 40–60 K the main product is solid-state CO_2. As the substrate temperature is increased above 60 K, the CO_2 is detected in the gas phase, and at even higher temperatures, that is, ≥ 90 K, O_2 formation is observed at the cost of CO_2.

6.4   Discussion

It is clear from the presented results that CO_2 is formed in our experiments, and that the temperature of the ASW influences the physical appearance of CO_2. In the following section we explore the different pathways to CO_2, which one results in the formation of CO_2 in our experiments, under which conditions, and what the efficiency is of this process.

6.4.1   Exploring the reaction network

In the introduction we mentioned several pathways that can form CO_2. The formation of CO_2 in our experiments is driven by VUV irradiation of ASW that interacts with gas-phase CO. This is different from most earlier studies where CO was embedded and intimately mixed with water ice. Such experiments are relevant for astronomical scenarios in which H_2O and CO are mixed in the solid state. However, these are not the scenarios discussed later in this paper, that is, protoplanetary disks (Section 6.5.1) and molecular cloud edges (Section 6.5.2).

There are two potential pathways to form CO_2 in our experiments, which involve both H_2O and CO, and three possible pathways that could lead to the observed formation of O_2 at higher temperatures. Figure 6.5 gives a schematic overview of the below described reactions.
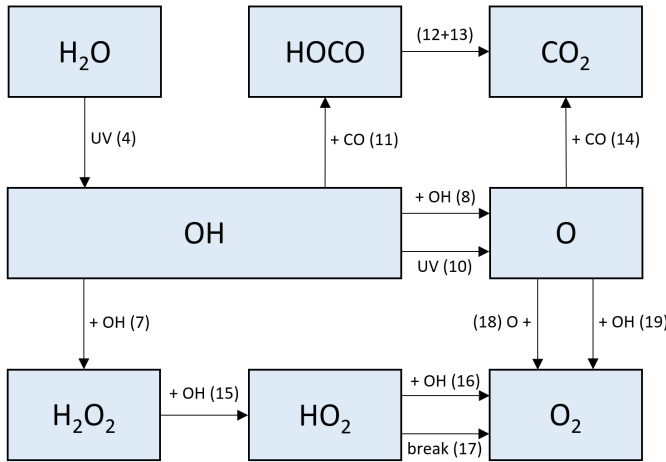
Figure 6.5: Schematic overview of the reactions that potentially occur in our experiments with VUV irradiation of solid-state H_2O in the presence of gas-phase CO. The numbers in parenthesis correspond to the reactions in Section 6.4.1. Backward, recombination, and by-products of reactions are not shown for clarity.

UV photons generally dissociate H_2O in the ice through its excited $\tilde{A}$ and $\tilde{B}$ states, which mainly lead to the formation of OH radicals and atomic oxygen,

$$H_2O + h\nu \rightarrow H + OH, \tag{6.3}$$

$$H_2O + h\nu \rightarrow H_2 + O(^1D). \tag{6.4}$$

Stief et al. (1975) reported quantum efficiencies of 0.89 and ≥ 0.99 for reaction (6.3), and quantum efficiencies of 0.11 and ≤ 0.01 for reaction (6.4) for the wavelength intervals 105-145 nm and 145-185 nm, respectively. In this study we use a MgF_2 window with no Lyman-α transmission between the MDHL and vacuum chamber. This ensures that Lyman-α photons are absorbed, and that the majority of the UV photons are in the 140–170 nm (7.3–8.9 eV) range, see Appendix 6.A. This, combined with the reported quantum efficiencies, results in the dissociation of H_2O only through the excited $\tilde{A}$, and produces OH radicals through reaction (6.3).

The formed H and OH proceed in different ways depending on the depth in the solid state at which dissociation occurs. The molecular dynamics calculations by Andersson & van Dishoeck (2008) showed that in the top three monolayers the majority of the photodissocation events results in the desorption of H and trapping of OH. At four monolayers or deeper most of the photodissocation events result in trapping of both species or recombination, reforming H_2O through reaction (6.5),

$$H + OH \rightarrow H_2O. \tag{6.5}$$

The desorption of H in the top three monolayers results in an enrichment of OH radicals on the surface. It was found in these calculations that the OH radicals can diffuse up to 60 Å on top of the H_2O surface at 10 K. This diffusion occurs on picosecond timescales, and does not include any thermal diffusion on longer timescales. Hama et al. (2009) showed that the OH radicals produced through reaction (6.3) are hot and have a translational temperature of 1300 ± 300 K. This significant amount of translational energy allows for additional diffusion, and increases the probability of two OH radicals to meet and react with each other. This reaction either forms hydrogen peroxide (H_2O_2) or H_2O and atomic oxygen, see reactions (6.6) and (6.7), respectively. The branching ratio between reactions (6.6) and (6.7) was found to be 0.8 and 0.2,

respectively, for two non-energetic OH radicals reacting with each other at 40–60 K (Oba et al. 2011),

$$OH + OH \rightarrow H_2O_2, \tag{6.6}$$

$$OH + OH \rightarrow H_2O + O(^3P). \tag{6.7}$$

As the abundance of the H_2O_2 increases, the amount of H_2O_2 dissociated by VUV photons increases through reaction (6.8),

$$H_2O_2 + h\nu \rightarrow OH + OH. \tag{6.8}$$

The translational temperature of these OH radicals was found to be 7500 ± 1000 K, which potentially allows for even further diffusion of OH radicals across the surface (Hama et al. 2009). These OH radicals on the surface, or those below for that matter, can be subsequently dissociated by VUV photons forming atomic hydrogen and oxygen, see reaction (6.9),

$$OH + h\nu \rightarrow H + O(^3P). \tag{6.9}$$

The OH radicals formed through reactions (6.3) and (6.8) are potential candidates for CO_2 formation when reacting with gas-phase CO. In the experimental study by Oba et al. (2010) the formation of CO_2 was observed from co-deposition of non-energetic OH radicals, cooled to 100 K prior to deposition, and CO molecules at 10 and 20 K. The authors proposed that CO_2 forms through reactions (6.10), (6.11), and (6.12),

$$CO + OH \rightarrow trans-HOCO, \tag{6.10}$$

$$trans-HOCO \rightarrow cis-HOCO, \tag{6.11}$$

$$cis-HOCO \rightarrow CO_2 + H. \tag{6.12}$$

Ground-state atomic oxygen formed through reactions (6.7) and (6.9) also has the potential to react with CO and form CO_2 through reaction (6.13),

$$CO + O(^3P) \rightarrow CO_2. \tag{6.13}$$

The addition of ground-state atomic oxygen to CO has been experimentally shown to work between 5 and 20 K, where CO is adsorbed on a bare substrate (Roser et al. 2001; Madzunkov et al. 2006; Raut & Baragiola 2011; Ioppolo et al. 2013). The same reaction has also been investigated on top of ASW by Minissale et al. (2013). These authors show that the CO_2 is formed through reaction (6.13) when CO and O are co-deposited on the surface of ASW in the temperature range 10–50 K.

The initially formed O, OH, and H_2O_2 can react with each other to form the hydroperoxyl radical (HO_2) and O_2. The HO_2 radical is formed through subsequent reactions of H_2O_2 with OH, see reaction (6.14). O_2 can be formed through different means, 1) an HO_2 radical reacts with OH, see reaction (6.15), 2) the HO_2 radical falls apart, see reaction (6.16), 3) atomic oxygen reacts with OH, see reaction (6.17), or 4) atomic oxygen reacts with another atomic oxygen, see reaction (6.18).

$$H_2O_2 + OH \rightarrow HO_2 + H_2O, \tag{6.14}$$

$$HO_2 + OH \rightarrow O_2 + H_2O, \tag{6.15}$$

$$HO_2 \rightarrow H + O_2, \tag{6.16}$$

$$O + OH \rightarrow O_2 + H, \tag{6.17}$$

$$O + O \rightarrow O_2. \tag{6.18}$$
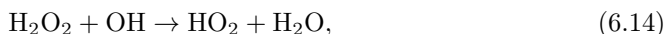
6.4.2 CO_2 formation pathway

In order to disentangle which of the above formation pathways is active in our experiments, we look at the following aspects: 1) the temperature dependence of CO_2 formation, 2) isotopologue behaviour, and 3) comparison with other work, available from literature. Across the temperature range of 40–90 K, the total column density of formed CO_2 is constant, but above 90 K the efficiency of CO_2 formation decreases due to the competing formation of O_2, see Figure 6.4. This temperature dependence contains significant amount of information, which allows us to constrain the formation of CO_2 to one pathway.

Our experiments show that CO_2 is formed through the reaction between gas-phase CO and solid-state OH radicals. These OH radicals are the primary product of H_2O dissociation in our experiments, and are thus most likely to react with CO. This particular reaction pathway to CO_2 has been investigated extensively (Watanabe & Kouchi 2002b; Watanabe et al. 2007; Ioppolo et al. 2009; Oba et al. 2010, 2011; Ioppolo et al. 2011; Noble et al. 2011; Zins et al. 2011; Yuan et al. 2014). However, the majority of these studies were performed at temperatures where CO is in the solid state, and mixed with H_2O. Oba et al. (2010) looked at the formation of CO_2 through co-deposition of CO and non-energetic OH radicals at a temperature of 10 and 20 K. Besides CO_2, the authors also observed the intermediate products cis- and trans-HOCO radicals at 1774 and 1812 cm^{-1}, respectively. They found that the HOCO absorption features disappear at $T > 40$ K, which is in line with the experimental work of Milligan & Jacox (1971). This is most likely the reason why the cis- and trans-HOCO radicals are not detected in the infrared spectra of our experiments (spectra not shown). In a follow-up study, Oba et al. (2011) investigated the same reactions, but in the temperature range 40–60 K. Formation of CO_2 was observed in the IR, but the efficiency at which CO was converted into CO_2 decreased with increasing temperature. The conversion rates were found to be 1.4%, 0.8%, and 0.3% at 40, 50, and 60 K, respectively. This decrease was attributed to the decreasing residence times with increasing surface temperature of both CO and OH. In our experiments this efficiency decrease is not observed, even when only considering solid-state CO_2. A possible explanation to this is the different origin of the OH radicals; in our work the radicals are formed *in situ*, whereas in previous studies OH radicals are deposited.

The other proposed formation pathway to CO_2 in which atomic oxygen reacts with gas-phase CO can be excluded. Given the temperature range, 40–120 K in which CO_2 is formed, and that O_2 is significantly formed at temperatures ≥ 90 K, it is unlikely that atomic oxygen is involved due to its short residence times, and that it is a secondary product of OH radicals through reactions (6.7) and (6.9) in our work. Additionally, on ASW atomic oxygen and CO have similar binding energies, that is, 1320 and 1350 K, respectively, and thus their residence times on the surface are comparable (Minissale et al. 2016; He et al. 2016a). Because of their similar residence times, no difference should be observed between the formation of CO_2 and O_2 with experimental temperature. However, as this difference is observed, this is additional proof that atomic oxygen is not involved in the formation of CO_2. Lastly, Minissale et al. (2013) investigated the formation of CO_2 through co-deposition of CO and atomic oxygen on top of ASW. It was found that the efficiency of CO_2 formation peaked at 35 K and dropped to zero at 60 K. As CO_2 formation is observed in our experiments up to 120 K, this is again evidence that atomic oxygen is not involved in the formation of CO_2. It should be noted that experimental conditions are not identical, as in our

experiments the atomic oxygen would be formed *in situ* instead of co-deposited with CO. However, since atomic oxygen is in the ground state, for both our work and that of Minissale et al. (2013), no clear differences are expected.

Formation of CO_2 through excited CO reacting with another CO molecule on the surface of ASW can also be ruled out. This is unlikely to occur, because it would require a CO molecule to be excited during its short, but nonzero, residence time and react with another CO molecule which has an equally short residence time. Additionally, in the control experiment with $H_2^{18}O$ and $^{13}C^{16}O$, the formed CO_2 is measured with the QMS during TPD at $m/z = 47$, corresponding to $^{13}C^{16}O^{18}O$, see Appendix 6.14. If the CO_2 is formed through excited CO and another CO molecule it is expected to be observed at $m/z = 45$, corresponding to $^{13}C^{16}O_2$.

From above results and discussion it is most likely that CO_2 is formed through the interaction between CO and OH radicals, formed by UV dissociation of H_2O. However, it is not yet clear if CO directly interacts with OH radicals from the gas phase, that is, an Eley-Rideal type reaction, or if CO adsorbs onto the ASW, diffuses, and subsequently reacts with OH radicals, that is, a Langmuir-Hinshelwood type reaction. Additionally, the formation location of CO_2 is also not yet clear; is it formed on the surface or embedded in the ASW? Both of these topics will be discussed in the following section.

6.4.3   The formation location of CO_2

It is possible to estimate the time a species resides on a surface given a temperature and binding energy to that surface. We derived that CO has residence times on ASW of 4.5×10^2–7.7×10^{-8} s in the range from 40 to 120 K. This is found through the Arrhenius equation, which can be written as

$$k = Ae^{-\frac{E_{bind}}{T}}, \tag{6.19}$$

where k is the rate constant, A the frequency factor, which is taken to be 10^{12} s^{-1}, E_{bind} the binding energy of a species to a specific surface in K, and T the temperature of the surface in K. The residence time is then given by the reciprocal of the rate constant from Eq. 6.19. For CO on ASW, the binding energy is dependent on the CO surface coverage, ranging from 1000–1700 K at 1–10^{-3} monolayer coverage, respectively (He et al. 2016a). The above residence times are estimated given an average binding energy of 1350 K for CO on ASW. For comparison, the binding energy of CO on the CO–CO interface is 855 ± 25 K (Öberg et al. 2005).

Even within these short residence times, some diffusion across the surface is expected. The number of binding sites CO visits on ASW, before desorption occurs, is estimated to be 7.2×10^{10}–4.2×10^3 in the range 40–120 K. This is also derived through Eq. 6.19. Specifically, the amount a CO can diffuse across different binding sites before a species desorbs is approximated by dividing the diffusion rate by the desorption rate. The diffusion rate is estimated by exchanging the E_{bind} term in Eq. 6.19 for the diffusion energy (E_{diff}). The rate constant is then a proxy of the number of hops a species makes between different binding sites per second. The diffusion energy for CO on ASW has recently been measured *in situ* with transmission electron microscopy (TEM), and was found to be 350 ± 50 K (Kouchi et al. 2020).

Given these residence times and amount of binding sites that are "visited" before desorption occurs, we conclude that CO spends sufficient time on the surface of ASW

to react with OH radicals through a Langmuir-Hinshelwood type reaction. This is different from Yuan et al. (2014), who investigated this reaction under similar experimental conditions and attributed it to an Eley-Rideal type of reaction. Yuan et al. (2014) employed a slightly higher binding energy of 0.125 eV (1450 K) for CO on H_2O, which results in a residence time of $\sim 2 \times 10^{-4}$ s at their experimental temperature of 76 K. The residence time is used to calculate the fractional coverage of CO on H_2O and was found to be 1×10^{-6} ML. The resulting fractional coverage of OH was derived to be 0.05 ML, over four orders of magnitude higher, which led to the conclusion of an Eley-Rideal type of reaction. However, diffusion of CO during this (short) residence time was not considered. At these temperatures, CO visits approximately 10^6 binding sites during its residence time, and thus, the effective surface scanned by CO is ~ 1 ML even though the fractional coverage of CO is only 1×10^{-6} ML. This supports that the involved mechanism follows a Langmuir-Hinshelwood type reaction.

Furthermore, we see no evidence of significant CO diffusion, and subsequent trapping, into the *bulk* of the H_2O ice. However, there is some trapping of CO in the surface and/or pores of the ASW. This is shown in a control experiment where ASW is exposed to CO molecules, but not to VUV irradiation. During TPD of this control experiment, as is shown in Appendix 6.15, the majority of the CO desorbs at approximately 50 K. Only a small amount of CO "volcano" desorbs when the ASW crystallizes. It is most likely that this CO got trapped in ASW due to pore collapse, instead of actually diffusing into the bulk ASW.

6.4.4   Temperature dependent formation, CO_2 vs O_2

Now that it is clear that the CO_2 in our experiments is formed through a Langmuir-Hinshelwood type reaction between solid-state OH radicals and solid-state CO molecules, be it with very short residence times, we can look at the reason why at temperatures > 90 K the CO_2 formation becomes less effective. Given the short residence time of atomic oxygen on ASW at temperatures > 90 K, that is, $< 2.3 \times 10^{-6}$ s, that atomic oxygen is a secondary product through reactions (6.7) and (6.9), and is not involved in the formation of CO_2 (see Section 6.4.2), we expect that atomic oxygen is also not involved in the observed formation of O_2 in our experiments.

This leaves the formation of O_2 involving a HO_2 radical, which is formed through the reaction of an OH radical with H_2O_2, reaction (6.14). This H_2O_2 is formed from two OH radicals through reaction (6.8). The formation of CO_2 and O_2 is thus both dependent on the availability of OH radicals. Given the temperature dependence it is likely that the mobility of the OH radical holds the answer to why these pathways are in competition. This is an interesting pathway to form O_2 at high temperatures, especially compared to the "standard" pathways with atomic oxygen, reactions (6.17) and (6.18). In this work we only explore this as a way to explain the decrease in CO_2 formation at temperatures > 90 K. A more in-depth investigation of this pathway to O_2 is beyond the scope of this work and will be presented in the near future.

6.4.5   Conversion rate of CO into CO_2

In order to demonstrate that the gas-grain pathway to convert CO into CO_2 is a process of importance in astrophysical environments, we discuss in this section its conversion rate and limiting factors. In total ~ 60 monolayers of water ice are deposited on the substrate in preparation of our experiments. However, as this conversion of CO into

CO_2 occurs on the surface, not all of this H_2O is available to act as a reacting medium. Classically, the surface of solid-state H_2O contains approximately 10^{15} molecules per cm^2. However, due to the porous nature of our ASW, the available H_2O surface for CO to adsorb on is expected to be larger. Additionally, with hydrogen released from the top three monolayers upon UV dissociation of H_2O, and the mobility of the OH radicals, we assume that OH radicals formed in the top three monolayers are available to convert CO into CO_2 (Andersson & van Dishoeck 2008). These top three monolayers, that is, 3.0×10^{15} H_2O molecules cm^{-2}, are henceforth the reactive surface.

In this reactive surface UV photons are absorbed by H_2O with an average VUV absorption cross section of $(3.4 \pm 0.2) \times 10^{-18}$ cm^2 (Cruz-Diaz et al. 2014). Given this cross section, roughly 1% of the total incident VUV fluence is absorbed by H_2O in the reactive surface, and equals 4.5×10^{16} photons. On the assumption that H_2O dissociation is 100% efficient, this produces an equal amount of OH radicals in the reactive surface. In the temperature range 40–90 K, approximately 2.7×10^{15} CO_2 molecules are formed, and thus an equal amount of OH radicals is consumed. This means that, for our assumptions, only 6% of the available 4.5×10^{16} OH radicals are involved in the conversion of CO into CO_2.

In our experiments OH, and not CO, is the limiting factor in the reaction. In the temperature range of 40–90 K, the formation of CO_2 is considered to be constant. However, the residence time of CO is lowered by a factor of 10^8 and the binding sites visited by CO by a factor of 10^5 from 40 to 90 K. That is to say, once CO finds an OH radical on the surface that is available, the conversion into CO_2 is (close to) unity.

The small fraction (6%) of UV absorption events resulting in CO_2 production, may be a consequence of inefficient H_2O dissociation or OH + H recombination. There is the possibility that 94% of the OH radicals are not good "candidates" for reacting with CO in this reactive surface. This would be surprising, because even non-energetic OH radicals in the ground state are able to form CO_2 with CO at 10 K (Oba et al. 2010). However, in the interest of the argument, lets assume that indeed 94% of the OH radicals do not convert CO into CO_2. This leaves an OH rich surface, since the hydrogen atoms desorb upon H_2O dissociation in this reactive surface. This large quantity of OH radicals should largely find each other and react to form H_2O_2 and O_2. The infrared does not show any of the vibrational modes of H_2O_2 within our detection limits (spectra not shown), especially not with the expected H_2O_2 column density of ~ 20 monolayers, and only at temperatures ≥ 90 K significant amounts of O_2 are observed, but only at column densities of ~ 3, not 20 monolayers (at 120 K; see Figure 6.4). In itself this column density is already questionable, as it is approximately seven times larger than the available H_2O molecules in this reactive surface. A control experiment where ASW is irradiated at 40 K and gas-phase CO is omitted, does show the formation of H_2O_2 and O_2, see Appendix 6.16. This shows that in the presence of gas-phase CO the formation of H_2O_2 and O_2 in the reactive surface is quenched, and that in the main experiments all available OH radicals react with CO into CO_2.

The amount of CO_2 produced, and lack of H_2O_2 and/or O_2 at T < 90 K, in the experiments is in conflict with the amount of OH radicals that should be produced with 100% dissociation efficiency of H_2O. Does not every VUV absorption event result in the dissociation of H_2O or is recombination after VUV dissociation a lot more efficient in our experiments? Fully answering this question is beyond the scope of this work, but it leads to a conundrum that requires future attention. It is unlikely that recom-

bination to H_2O is significantly more efficient than predicted by molecular dynamics calculations. Photodissociation and desorption occur on picosecond timescales after UV absorption in these simulations, and thus, diffusion of atomic hydrogen within this time window is improbable. It should be noted that in molecular dynamics calculations only a single event is considered per simulation, and thus for H_2O recombination to occur the atomic hydrogen needs to find its original OH partner before it desorbs. It could be that in our experiments the atomic hydrogen reforms H_2O with previously formed OH radicals due to the high UV photon fluxes 2.5×10^{14} photons s^{-1} cm^{-2}. Molecular dynamics calculations of H_2O photodissociation and recombination with neighbouring OH radicals are needed to test the efficiency of this channel.

The lack of efficient H_2O recombination points toward inefficient photodissociation of H_2O upon absorption of a UV photon in the excited $\tilde{A}$ state. However, in Figure 2 of Andersson & van Dishoeck (2008) the fraction probabilities of photodissociation pathways for H_2O are given per *absorbed* photon and sum to (near) unity. This is in conflict with our results as we only observe 6% (effective) dissociation efficiency of H_2O. Schriever et al. (1990) investigated the absolute photodissociation quantum yield of H_2O in an argon matrix (ratio 1:500). It was found that at 160 nm and 5 K the photodissociation efficiency of isolated H_2O in argon equals 20–30%. It should be noted that in the work by Schriever et al. (1990) the H_2O is isolated and trapped in the bulk, which cannot necessarily be extrapolated to our work. However, it does hint that photodissociation of H_2O with VUV, under laboratory conditions, is not 100%. More investigation is needed here, as this is key for a correct incorporation of the laboratory results into astrochemical models.

Interestingly, the molecular dynamics calculations by Arasa et al. (2013) find a similar conversion factor, that is, ~ 0.03 per absorbed photon, for the interaction between CO and OH. In their work different CO-H_2O systems were investigated, where H_2O was dissociated through the first excited state with ultraviolet photons at 10 K. They found that CO needs to be embedded in H_2O for it to be converted into CO_2 with a probability of $(3.6 \pm 0.7) \times 10^{-4}$ per absorbed photon. However, it was found that the intermediate HOCO complex has a significant higher formation probability of $(3.00 \pm 0.07) \times 10^{-2}$ per absorbed photon. This was explained by the HOCO complex being trapped in the solid state and losing its internal energy to the surrounding molecules, which prevents further reaction to CO_2 + H. In our experiments the HOCO complex is not observed. However, it could very well be that this HOCO complex still is involved in the formation of CO_2 in our experiments due to the increased ASW temperature, as seen in Milligan & Jacox (1971) and Oba et al. (2011). If this is the case, then our formation efficiency of 0.06 per absorbed photon is in agreement with that from Arasa et al. (2013). It should be noted that the authors assume that each absorbed photon leads to dissociation into H and OH.

Although our formation efficiency is comparable to that of Arasa et al. (2013), the motivation is different. In the molecular dynamics calculations the location and orientation of the reaction products are the limiting factor, while in our experiments, due to the lack of other reaction products, it seems that photodissociation of H_2O in the solid state is not efficient. A possible source of error in our determination of the formation efficiency are the experimental assumptions. Using Gaussian error propagation, we estimate the error in our formation efficiency of CO_2 per *absorbed* VUV photon in the reactive surface to be 60%, and thus ranges from 2–10%.
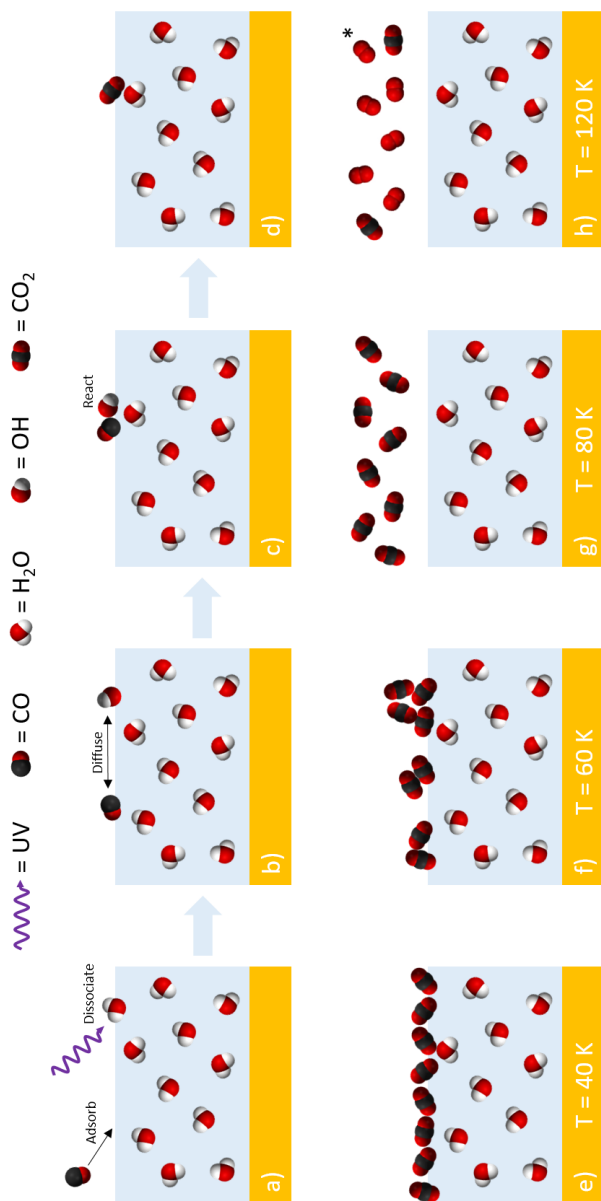
Figure 6.6: Simplistic representation of the processes that occur in our experiments. Panel a) through d) show the proposed Langmuir-Hinshelwood reaction that creates CO_2 in our experiments. Panels in the bottom row schematically show the structure or phase in which the formed products end up after formation, given a certain experimental temperature. $^{(*)}$ Molecular oxygen is not formed through the depicted reaction, for details see Section 6.4.1 & 6.4.4.

6.5   Astrophysical implications

The above results and discussion are summarized in a simplified cartoon (see Figure 6.6). In the top row of this figure, the formation process is visualized. Formation of CO_2 on the surface of ASW through VUV irradiation of H_2O and interaction with gas-phase CO is discussed in detail in Section 6.4. In short, CO has a short, but nonzero, residence time on ASW even though its temperature is above the canonical desorption temperature of CO. This combined with VUV irradiation of H_2O results in the formation of OH radicals. The diffusion of CO and OH radicals allows them to react with each other and form CO_2 in a Langmuir-Hinshelwood type reaction. The bottom row of Figure 6.6 illustrates the physical appearance of the formed CO_2 with changing substrate temperature. A full analysis of the experiments is given in Section 6.3, but briefly, in the lower end of the experimental temperature range, that is, 40–60 K, the formed CO_2 remains in the solid state. Specifically, at 40 K (Figure 6.6e) the CO_2 is not mobile enough and the majority of the CO_2 stays bound to the ASW surface. However, in the experiment at 60 K (Figure 6.6f), the CO_2 has significant mobility and starts diffusing across the surface, and forms CO_2 cluster islands on top of the ASW. As shown in Figure 6.6g, the formed CO_2 is released into the gas phase at 80 K, and at higher temperatures, the formation of O_2 starts competing with CO_2, which is shown in Figure 6.6h. In the 40–90 K range, our experiments show that 2–10% of the *absorbed* UV photons in the reactive surface, that is, top three monolayers of ASW, result in the conversion of gas-phase CO into CO_2. In the following section, we look at two astrophysical environments, that is, protoplanetary disks and molecular clouds, where this pathway could play an important role.

6.5.1   CO conversion in protoplanetary disks

In planet forming disks, the gas mass, as derived through CO isotopologues, often comes out factors 10–100 lower than expected based on the dust content. This finding is based on physical-chemical modeling that includes photodissociation and freeze out of CO and its isotopes (Miotello et al. 2014, 2016, 2017). One interpretation is that these disks have already lost a significant fraction of their total gas mass. Another is that some unknown process locks up gas-phase CO on grains. A correct interpretation is essential for models of planet formation that rely on the available gas-mass reservoir as well as on the gas-to-dust ratio. Other gas-mass tracers are problematic, as H_2 is undetectable and HD has only been observed in a few sources (see e.g., Bergin et al. 2013; McClure et al. 2016; Trapman et al. 2017; Kama et al. 2020), where, incidentally, the HD data support the notion of gas-phase CO being locked up. The CO into CO_2 conversion has been proposed as a possible pathway to convert gas-phase CO into a species that is much more difficult to detect.

Chemical-modeling work by Bosman et al. (2018) looked at several pathways through which CO could be converted into less volatile species to explain the low observed CO fluxes. These models are successful in this conversion on timescales shorter than average protoplanetary disk lifetimes, that is, ~ 3 Myr. It should be noted that it was found in these models that gas-phase CO is in competition with atomic hydrogen for OH radicals on the surface (see Bosman et al. 2018, for more details). Furthermore, these results depend on the adopted binding energies, reaction rates, and formation of H_2. For example, the binding energy of CO in these models is

kept constant at 855 K, no matter the environment. However, it has been found that the binding energy of CO on ASW can be as high as 1700 K (He et al. 2016a). In a similar fashion, Trapman et al. (2021) used `DALI` models to investigate the low CO fluxes in the Lupus star-forming region. Disk regions with $T_{\mathrm{gas}} > 35$ K were excluded in these models for gas-phase CO conversion, as verification models showed that CO conversion through grain-surface chemistry was negligible at these temperatures, but again this was tested with a CO binding energy of 855 K.

Including the correct binding energy for CO on ASW in these types of models is crucial. This increased binding energy will allow gas-phase CO to compete with atomic hydrogen for OH radicals in a larger temperature range, and thus a larger region in protoplanetary disks where CO can be removed from the gas phase. In our experiments and the models by Bosman et al. (2018) and Trapman et al. (2021), the amount of gas-phase CO that is converted into CO_2 depends on the availability of OH radicals. The authors assume in their models that once H_2O absorbs an UV photon, dissociation is 100% efficient. As discussed in Section 6.4.5, our experiments show an efficiency for OH production of 2–10% per absorbed UV photon as opposed to the 100% adopted in the models. Further modeling is required, also including the correct binding energy of CO on ASW, to fully assess the impact of our results on the model predictions.

6.5.2 CO_2 formation in edges of molecular clouds

Observations of icy grains surrounding young stars suggest that large amounts of the solid-state CO_2 are embedded in a water-rich environment. Here we explore if the conversion of gas-phase CO into solid-state CO_2 could explain the puzzling presence of this solid-state CO_2. It is generally assumed that the ice that covers dust grains is composed of two layers: a polar and an apolar layer, where the apolar layer is on top of the polar layer (see e.g., Boogert et al. 2015). A polar ice layer is dominated by species with larger dipole moments, such as H_2O, and an apolar ice layer mainly contains species with smaller or no dipole moments, such as CO and N_2. The *Spitzer* "Cores to Disks" program showed that in embedded young low-mass stars the majority of the observed solid-state CO_2 is mixed in a polar water-rich environment (Pontoppidan et al. 2008). Given this H_2O-dominated environment, it is possible that a substantial fraction of this CO_2 is formed through reactions between CO and OH radicals. This would require CO to freeze out during H_2O formation in order to be intimately mixed and subsequently to be converted into CO_2.

Infrared observations show that it is unlikely that CO is mixed in a water-rich environment. The observed CO absorption feature can be deconvolved into three components, namely 4.665 μm (2143.7 cm^{-1}), 4.673 μm (2139.7 cm^{-1}), and 4.681 μm (2136.5 cm^{-1}). The blue component (4.665 μm) is assigned to CO in an apolor environment, specifically, it is linked to mixtures of solid-state CO and CO_2 (Boogert et al. 2002; van Broekhuizen et al. 2006) or crystalline CO (Pontoppidan et al. 2003). The middle component (4.673 μm) is generally attributed to pure CO (see e.g., Boogert et al. 2002). The red component (4.681 μm) has a broader "footprint" compared to the other two and is linked to CO in a polar environment. This polar environment could be H_2O and would set the scene for solid-state formation of CO_2 in a polar environment. However, Sandford et al. (1988) showed that if CO would reside in H_2O, one can expect a feature at 4.647 μm (2151.9 cm^{-1}) due to the dangling OH

bond, which has not been seen in interstellar spectra. It is thus unlikely that this CO is mixed with H_2O. Mixtures of CO with CH_3OH, however, do reproduce the red component in both peak position and width (Cuppen et al. 2011). A mixture of CO and CH_3OH is also more likely, as CH_3OH is formed through hydrogenation of CO (Hiraoka et al. 1994, 2002; Watanabe & Kouchi 2002a; Hidaka et al. 2004; Watanabe et al. 2004; Fuchs et al. 2009).

In order to explain the solid-state CO_2 embedded in water-rich environments without invoking the need for CO embedded in H_2O ice, we look at the initial build-up of water ice on dust grains. Water can be formed through both gas-phase and solid-state pathways. However, the gas-phase ion-molecule chemistry produces only a fraction of the total observed water abundances, and thus water is mainly formed through the addition of hydrogen to atomic oxygen on the surface of dust grains (see reviews by van Dishoeck et al. 2014; Linnartz et al. 2015, and references therein). This formation process of solid-state H_2O takes place in the edges of molecular clouds at intermediate extinction (A_V). At this extinction, CO is already present, but still resides in the gas phase. For example, in the Taurus molecular cloud water ice is detected at a threshold extinction, that is, the extinction at which a species is detected in the solid state, of 3.2 ± 0.1 A_V, while for CO the threshold extinction was determined to be 6.7 ± 1.6 A_V (Whittet et al. 2001, 2010). Physical-chemical models of molecular clouds show that the dust-grain temperature at the edge of a cloud equals 31 K, with an external FUV field strength of 100 G_0, where G_0 is a scaling factor in multiples of the average local interstellar radiation field, which is indeed sufficient to keep CO in the gas phase (Hollenbach et al. 2009). For CO_2 to be mixed with H_2O it has to form simultaneously, and since CO is in the gas-phase during H_2O formation, CO_2 can be formed through the process described in this work. The OH radicals required for the conversion of CO into CO_2 are readily available in this region. They are the intermediate product to H_2O formation, and the external UV field is still sufficient at this extinction to photodissociate already existing H_2O molecules.

The solid-state CO_2 that is observed to be embedded in water-rich environment in the "Cores to Disks" program, has a relative average abundance w.r.t. H_2O of ~ 0.2. Assuming that roughly equal amounts of atomic oxygen go into CO and H_2O, this would imply that approximately 20% of the gas-phase CO would have to be converted into solid-state CO_2 to explain observed abundances. Inclusion of this pathway in physical-chemical models of molecular clouds is required to test how efficient this process is in low-density regions at interstellar timescales and explain the observed solid-state CO_2 abundances.

6.6   Conclusions

In this study we investigate the interaction of gas-phase CO with vacuum-UV irradiated water ice. The temperature of the water ice is varied between 40–120 K, and several control experiments are performed to narrow down the possible interpretations of the results. Our findings are summarized as follows:

1. The interaction between gas-phase CO and vacuum-UV irradiated water ice produces CO_2 up to 120 K. Solid-state CO_2 is observed in the temperature range 40–60 K. At 70 K or higher, the formed CO_2 is released into the gas phase, and above 90 K, O_2 formation is observed at the cost of CO_2 production.

2. CO has a significant residence time on water ice, even though it is above the canonical sublimation temperature of CO. In this short, but nonzero, residence time, each CO is able to diffuse between up to 7.2×10^{10} different binding sites before desorption occurs. This significant diffusion allows CO to find an OH radical, created by UV dissociation of H_2O, and form CO_2 in a Langmuir-Hinshelwood type reaction.

3. Given that gas-phase CO can only interact with the surface of the water ice, this includes pores exposed to the vacuum, we derived a conversion rate of 0.06 per *absorbed* photon in the reactive surface (i.e., three monolayers). The limiting factor in this conversion rate is the production of OH radicals.

4. It is unclear what sets the efficiency of 2–10% of produced CO_2 per absorbed UV photon in the reactive surface, given that no other products, such as H_2O_2, are observed and molecular dynamics calculations indicate that photodissocation is (close to) unity and reformation into H_2O is inefficient.

5. Understanding this process is important for astrophysical regions, such as molecular clouds and planet-forming disks. In clouds, this processs can explain the presence of solid-state CO_2 embedded in water-rich ices. In disks, it has been invoked to explain the lack of gas-phase CO, but our results suggest that the laboratory efficiency of the process falls short to significantly reduce the observed gas-phase CO in protoplanetary disks.

This work demonstrates the wide temperature efficacy of this gas and grain interaction process. Future work, should focus on further experimental and theoretical exploration of the molecular dynamics which include the effects of high fluxes and neighbouring OH radicals on the reforming of H_2O after photodissociation. Additionally, these processes should be included quantitatively in models of planet-forming disk chemistry and molecular clouds. With this work we show that gas and grain chemistry cannot be considered as fully separate, but that, under the right conditions, interaction of the gas with the icy surface results in observable effects.

Appendix

6.A   UV spectrum

The spectral energy distribution of the MDHL used in this study is measured *in situ* with a VUV spectrometer (McPherson Model 234/302), which is mounted opposite to the MDHL on the other side of the main chamber. In this work a MgF_2 window was used that does not transmit Lyman-α photons, but does transmit the molecular hydrogen emission lines and continuum between 140–170 nm. The VUV spectrum with which the ASW is irradiated in our experiments is shown in Figure 6.7.
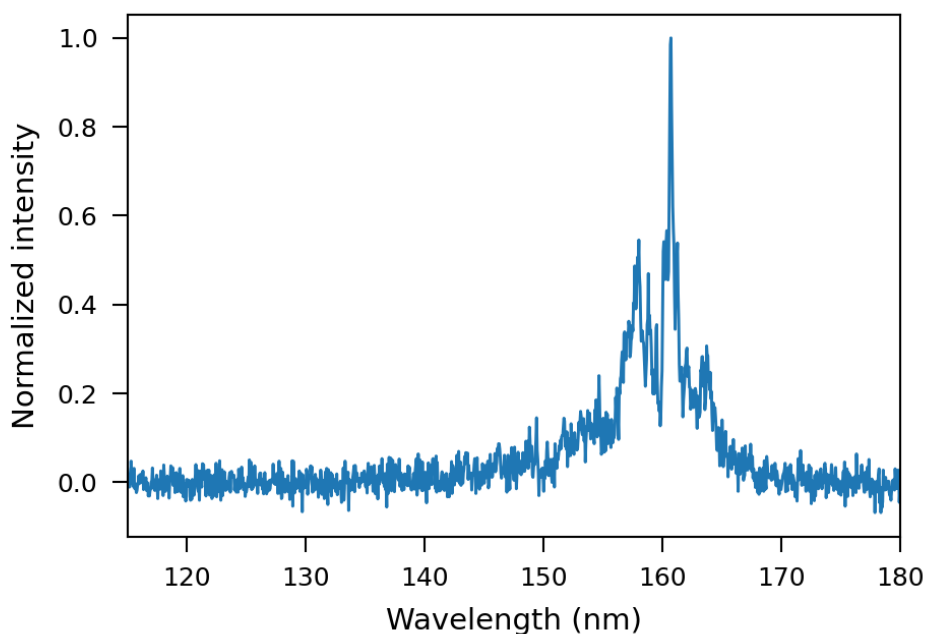
Figure 6.7: UV spectrum of the microwave discharge hydrogen lamp used in our work in combination with a MgF_2 window that absorbs Lyman-α.

6.B   Additional experiments

The main experiments at 50, 60, 80, 90, 100, and 120 K and control experiments with ^{13}CO instead of $^{13}C^{18}O$, no VUV irradiation, and no gas-phase CO are presented in this appendix. Due to a nonlinear temperature artifact during TPD, the majority of the experiments show an unexpected and erroneous signal increase in the QMS TPD panels (d). This occurs approximately in the temperature range 120–150 K. In the caption of each figure the exact temperature range is given in which the QMS signals are not reliable.
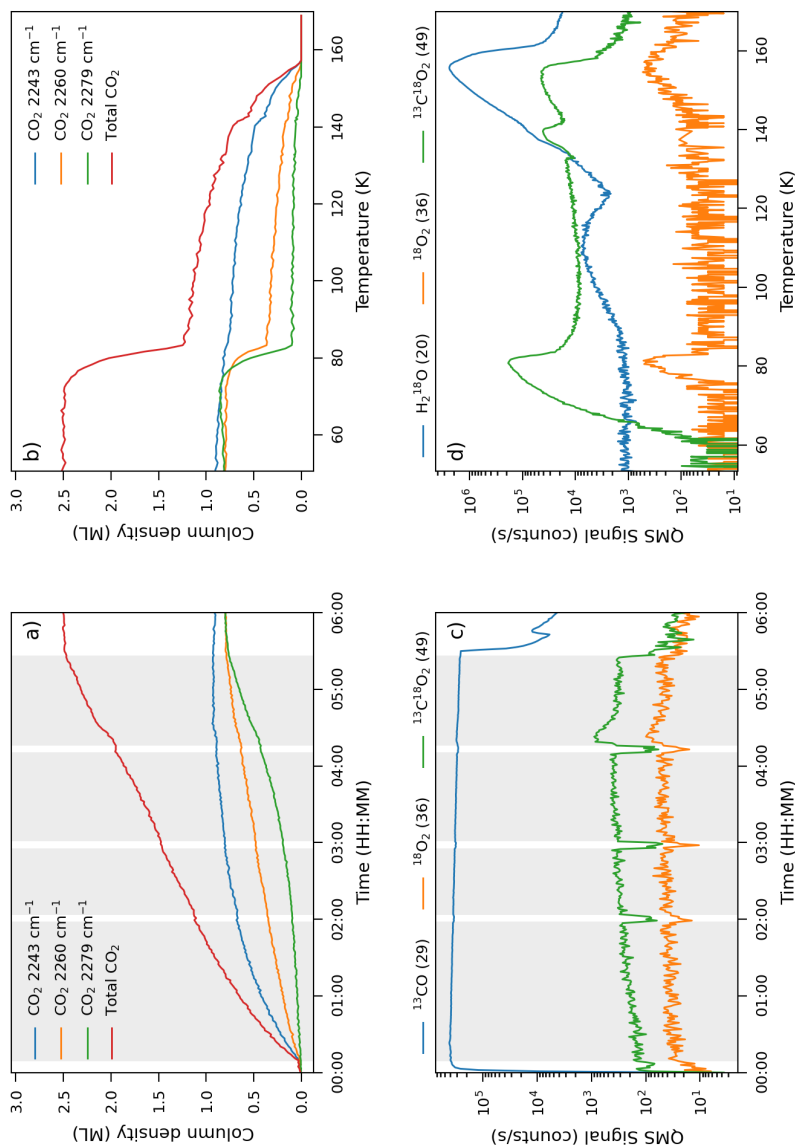
Figure 6.8: Results of the experiment of ASW at a temperature of 50 K. In the top row the deconvolved infrared components are given and in the bottom row the data for the quadrupole mass spectrometer (QMS) is presented. The left column shows data acquired during VUV irradiation (shaded area is with VUV shutter open) and on the right during temperature programmed desorption (TPD). ^{13}CO is shown in panel c), as measuring the main isotope ($^{13}C^{18}O$) would saturate the QMS and the ^{16}O isotope is present in the CO sample at a level of 5%. The increased signal in panel d) during the TPD between 130–140 K is due to nonlinear temperature artifact.
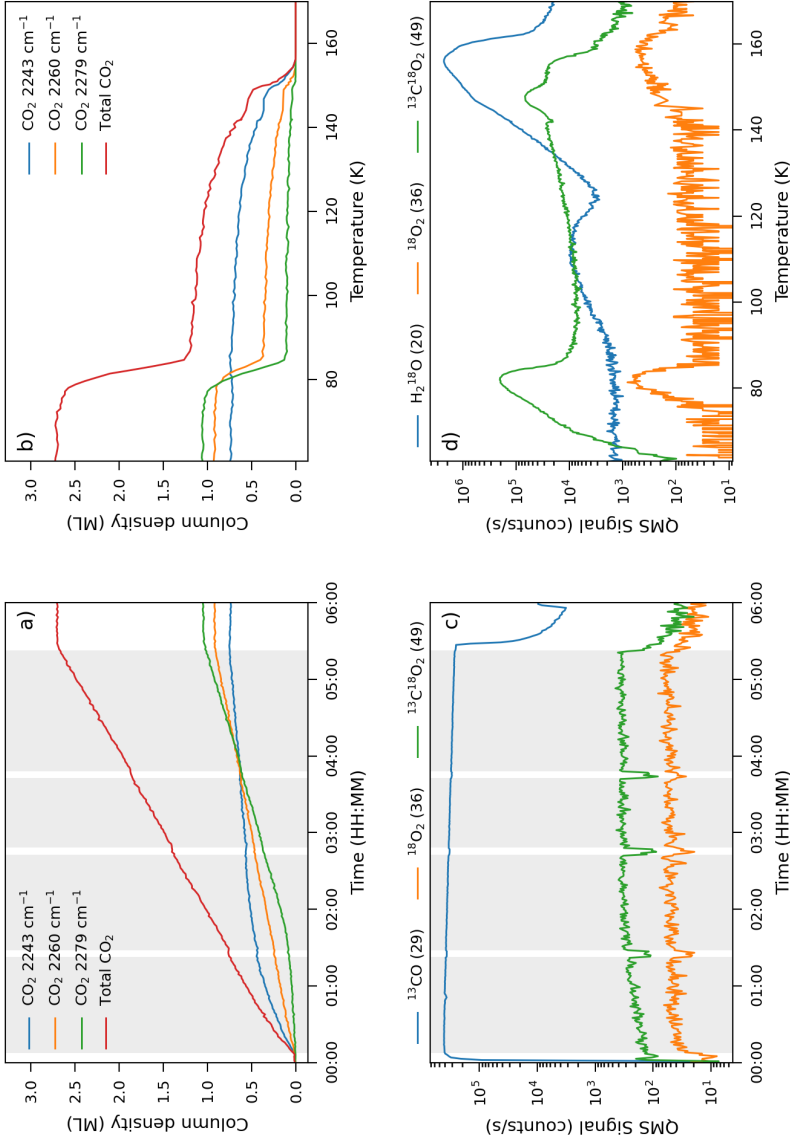
Figure 6.9: Results of the experiment of ASW at a temperature of 60 K. In the top row the deconvolved infrared components are given and in the bottom row the data for the quadrupole mass spectrometer (QMS) is presented. The left column shows data acquired during VUV irradiation (shaded area is with VUV shutter open) and on the right during temperature programmed desorption (TPD). ^{13}CO is shown in panel c), as measuring the main isotope ($^{13}C^{18}O$) would saturate the QMS and the ^{16}O isotope is present in the CO sample at a level of 5%. The increased signal in panel d) during the TPD between 140–150 K is due to nonlinear temperature artifact.
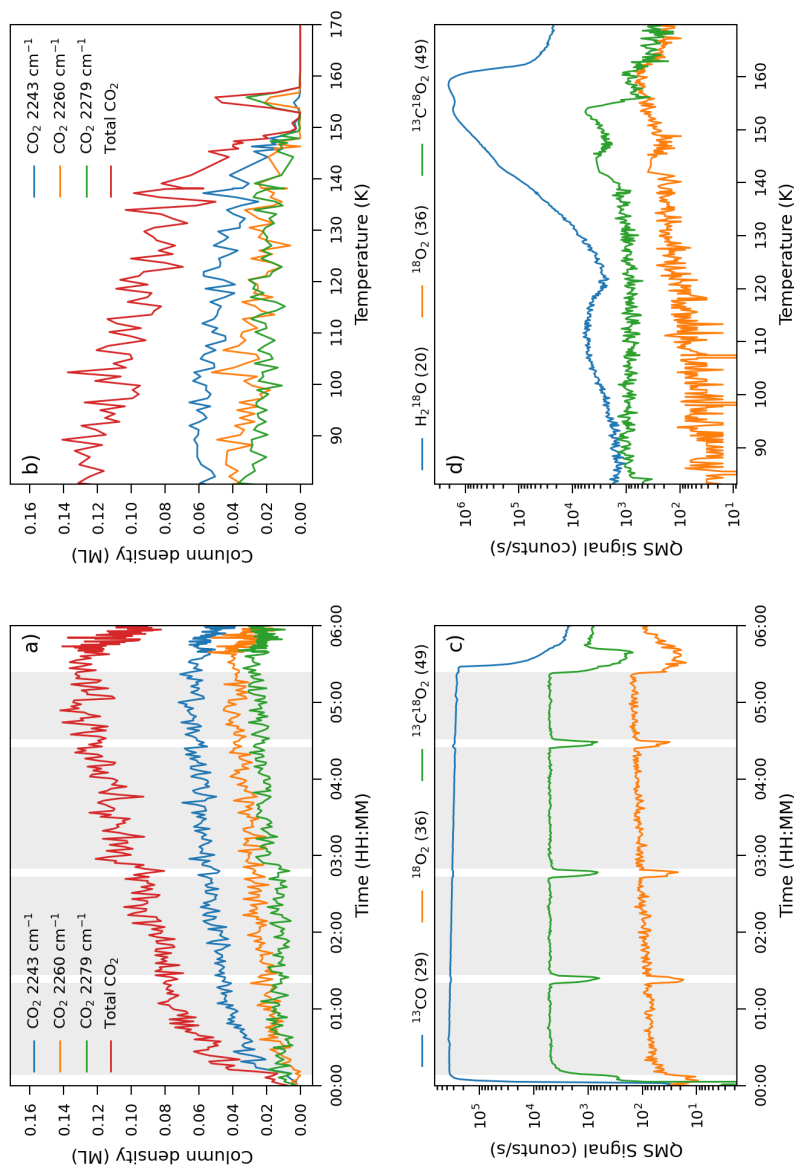
Figure 6.10: Results of the experiment of ASW at a temperature of 80 K. In the top row the deconvolved infrared components are given and in the bottom row the data for the quadrupole mass spectrometer (QMS) is presented. The left column shows data acquired during VUV irradiation (shaded area is with VUV shutter open) and on the right during temperature programmed desorption (TPD). ^{13}CO is shown in panel c), as measuring the main isotope ($^{13}C^{18}O$) would saturate the QMS and the ^{16}O isotope is present in the CO sample at a level of 5%. The increased signal in panel d) during the TPD between 140–150 K is due to nonlinear temperature artifact.
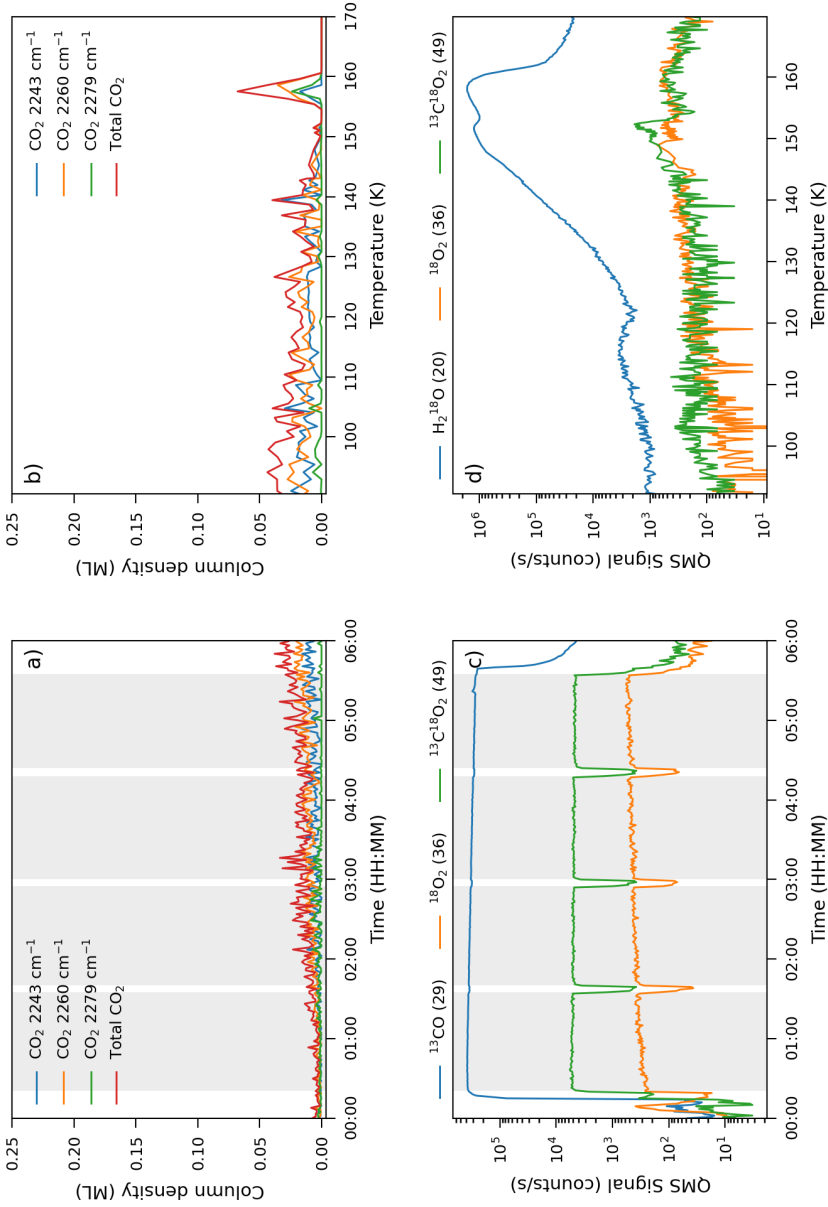
Figure 6.11: Results of the experiment of ASW at a temperature of 90 K. In the top row the deconvolved infrared components are given and in the bottom row the data for the quadrupole mass spectrometer (QMS) is presented. The left column shows data acquired during VUV irradiation (shaded area is with VUV shutter open) and on the right during temperature programmed desorption (TPD). ^{13}CO is shown in panel c), as measuring the main isotope ($^{13}C^{18}O$) would saturate the QMS and the ^{16}O isotope is present in the CO sample at a level of 5%.
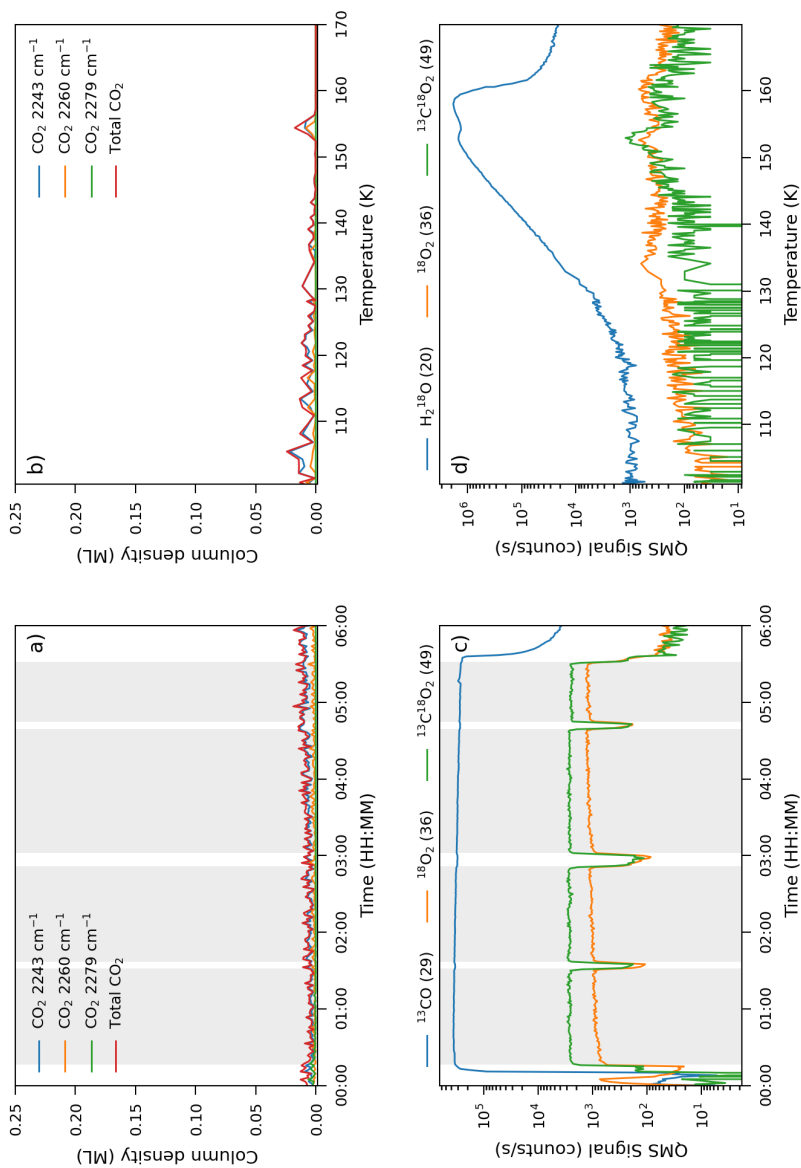
Figure 6.12: Results of the experiment of ASW at a temperature of 100 K. In the top row the deconvolved infrared components are given and in the bottom row the data for the quadrupole mass spectrometer (QMS) is presented. The left column shows data acquired during VUV irradiation (shaded area is with VUV shutter open) and on the right during temperature programmed desorption (TPD). ^{13}CO is shown in panel c), as measuring the main isotope (^{13}C^{18}O) would saturate the QMS and the ^{16}O isotope is present in the CO sample at a level of 5%. The increased signal in panel d) during the TPD between 130–140 K is due to nonlinear temperature artifact.
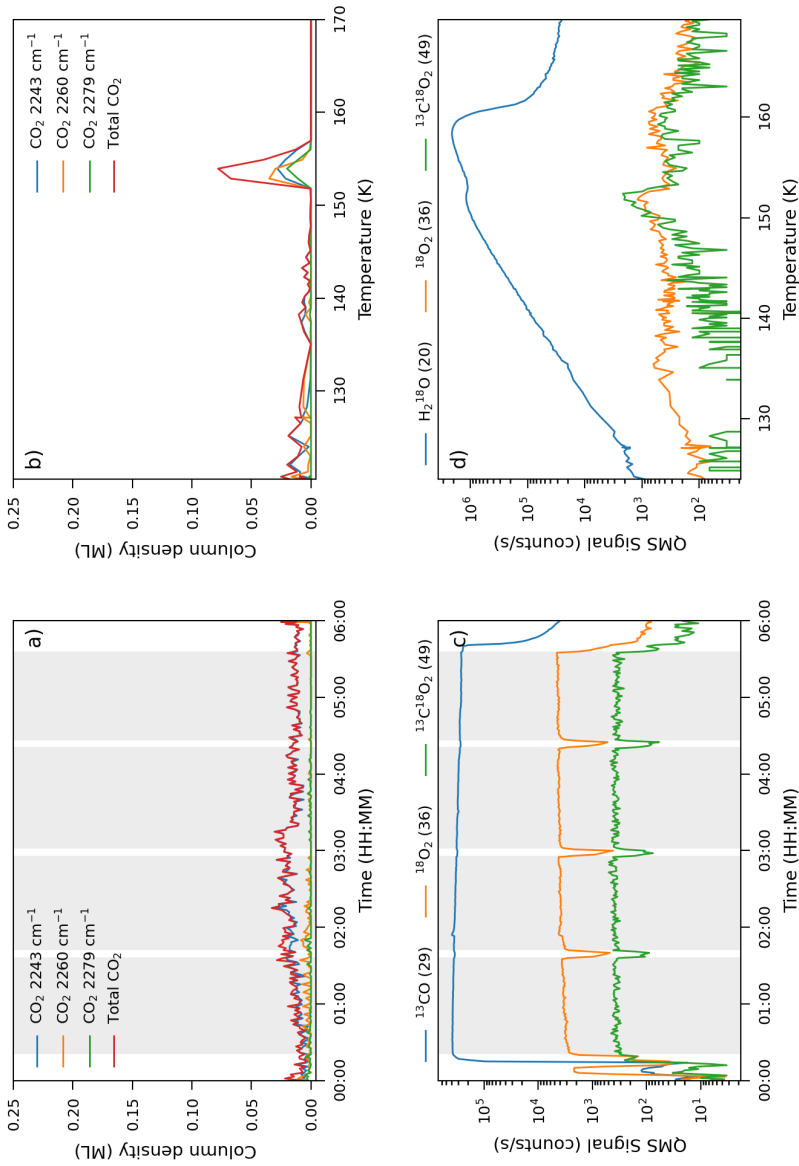
Figure 6.13: Results of the experiment of ASW at a temperature of 120 K. In the top row the deconvolved infrared components are given and in the bottom row the data for the quadrupole mass spectrometer (QMS) is presented. The left column shows data acquired during VUV irradiation (shaded area is with VUV shutter open) and on the right during temperature programmed desorption (TPD). ^{13}CO is shown in panel c), as measuring the main isotope ($^{13}C^{18}O$) would saturate the QMS and the ^{16}O isotope is present in the CO sample at a level of 5%. The increased signal in panel d) during the TPD between 130–140 K is due to nonlinear temperature artifact.
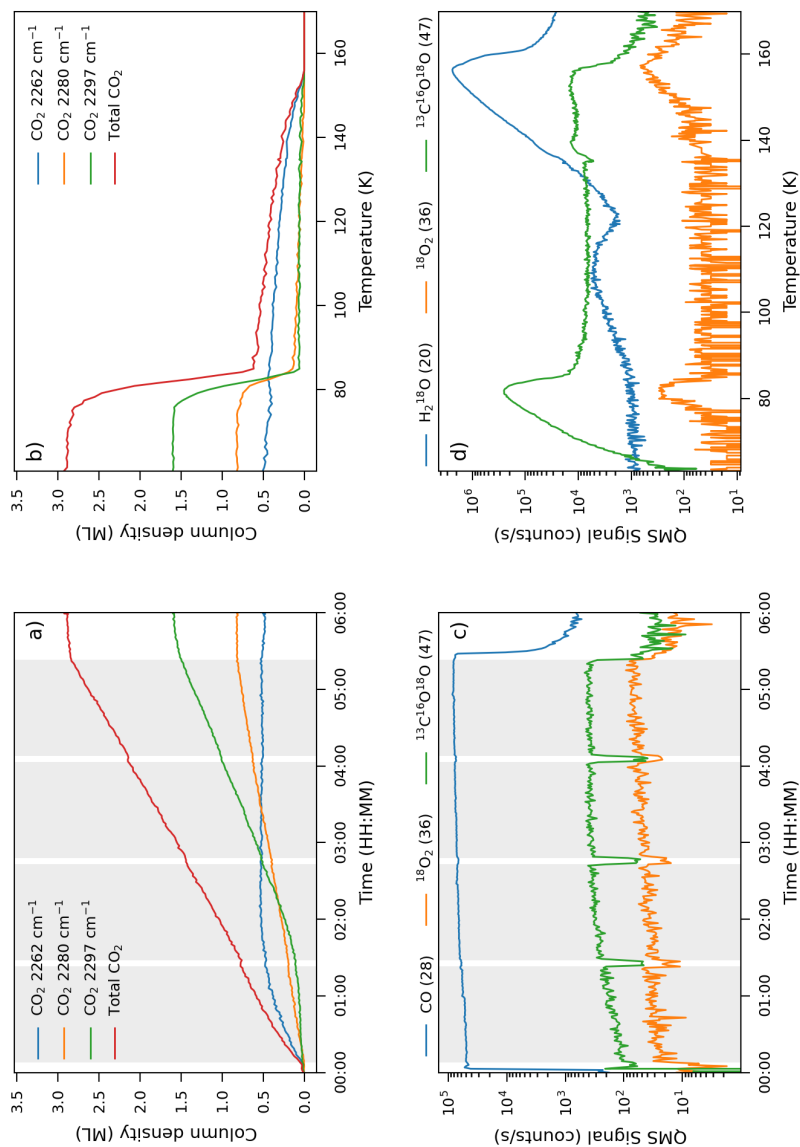
Figure 6.14: Results of the experiment of ASW at a temperature of 60 K with isotopic ^{13}CO instead of ^{13}C^{18}O. In the top row the deconvolved infrared components are given and in the bottom row the data for the quadrupole mass spectrometer (QMS) is presented. The left column shows data acquired during VUV irradiation (shaded area is with VUV shutter open) and on the right during temperature programmed desorption (TPD). ^{12}CO is shown in panel c), as measuring the main isotope (^{13}CO) would saturate the QMS and the ^{16}O isotope is present in the CO sample at a level of 5%. The increased signal in panel d) during the TPD between 130–140 K is due to nonlinear temperature artifact.
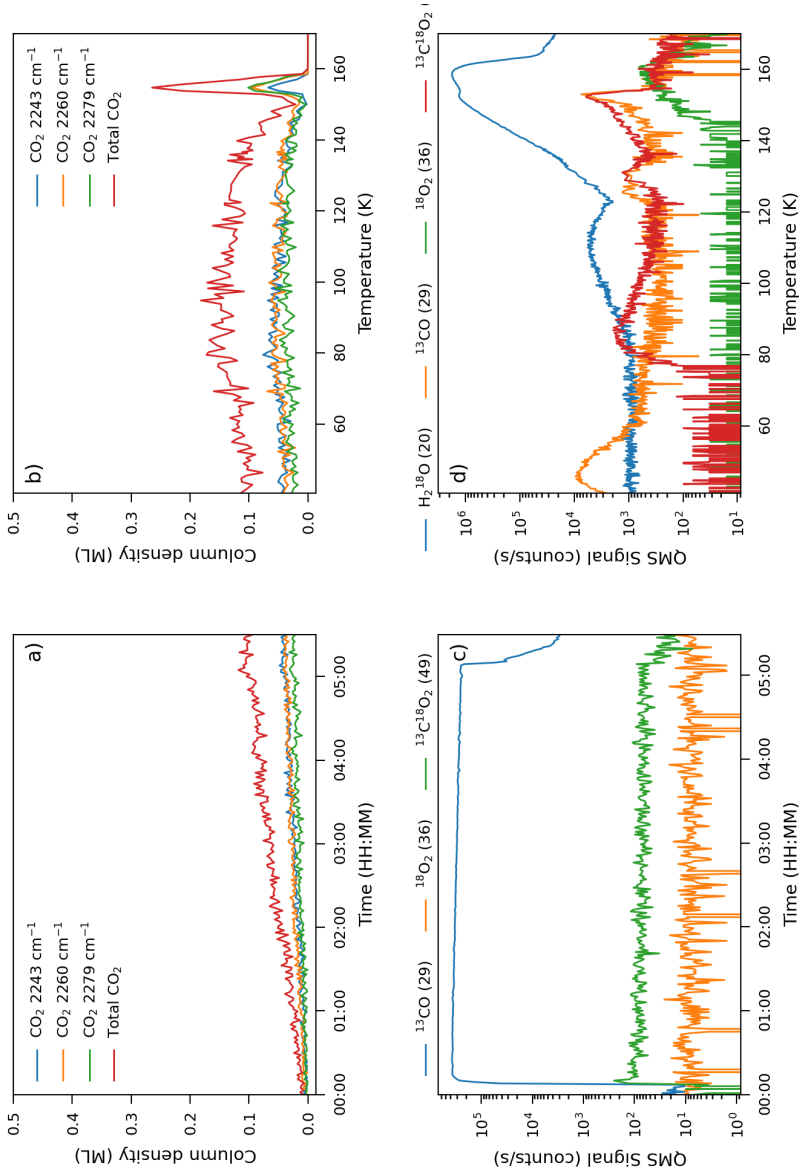
Figure 6.15: Results of the experiment of ASW at a temperature of 40 K without VUV irradiation. In the top row the deconvolved infrared components are given and in the bottom row the data for the quadrupole mass spectrometer (QMS) is presented. The left column shows data acquired during VUV irradiation (shaded area is with VUV shutter open) and on the right during temperature programmed desorption (TPD). ^{13}CO is shown in panel c), as measuring the main isotope (^{13}C^{18}O) would saturate the QMS and the ^{16}O isotope is present in the CO sample at a level of 5%.
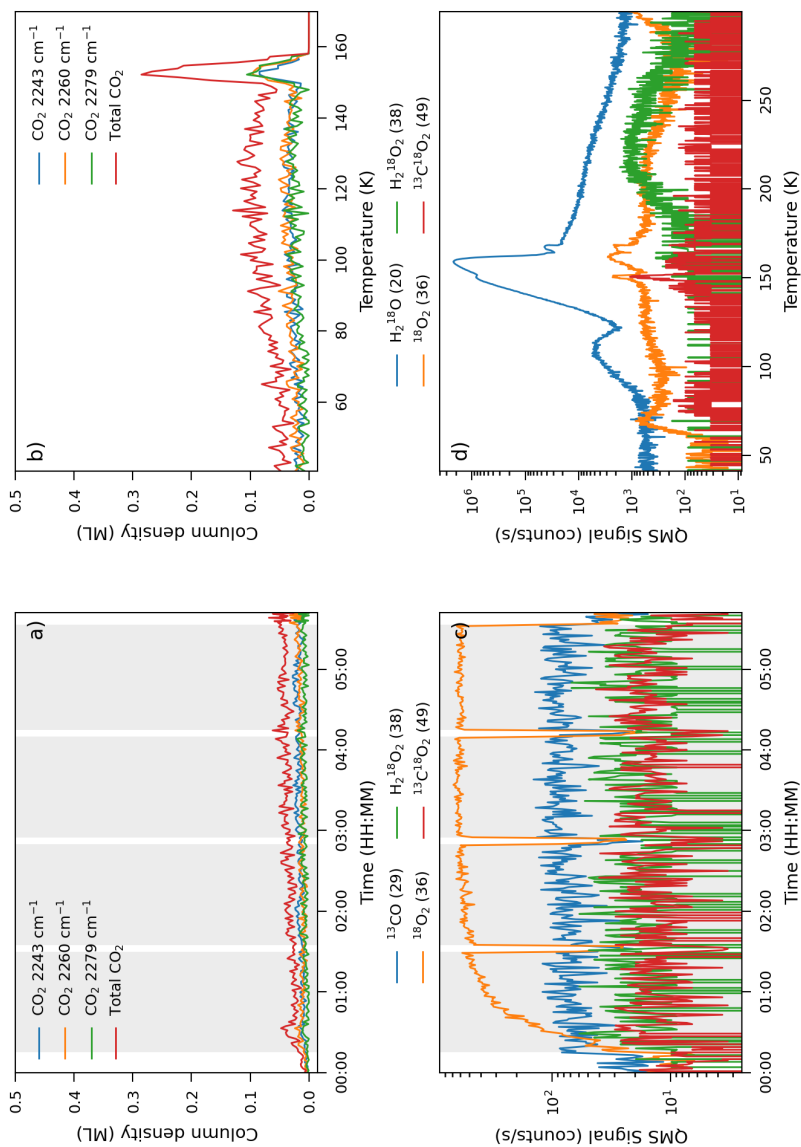
Figure 6.16: Results of the experiment of ASW at a temperature of 40 K without gas-phase CO. In the top row the deconvolved infrared components are given and in the bottom row the data for the quadrupole mass spectrometer (QMS) is presented. The left column shows data acquired during VUV irradiation (shaded area is with VUV shutter open) and on the right during temperature programmed desorption (TPD). TPD is now shown up until 300 K to show the desorption of H_2O_2. ^{13}CO is shown in panel c), to verify that indeed no significant amount of CO is in the gas phase during VUV irradiation.